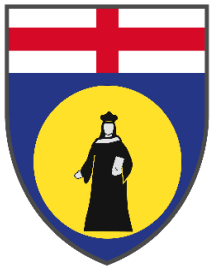

ITALIAN HYDROGRAPHIC INSTITUTE

in cooperation with the

UNIVERSITY OF GENOVA
(UNIVERSITÀ DEGLI STUDI DI GENOVA)

DEPARTMENT OF EARTH, ENVIRONMENT AND LIFE SCIENCES

MASTER'S DEGREE IN HYDROGRAPHY AND OCEANOGRAPHY

REMOTE DERIVED BATHYMETRY IN COASTAL AND RIVER MOUTH SHALLOW WATER: CASE STUDIES IN WESTERN LIGURIA

Supervisors
Prof.ssa Bianca Federici – UniGE
Dott. Alfonso Quarati – C.N.R. IMATI
Dott.ssa Lorenza Apicella – C.N.R. IMATI / UniGE

Candidate
Matteo Bozzano

Introduction

Discovering the subject

Navigation is not something everybody experiences in everyday life. The feeling of the ocean is usually meant for others. The cities we thrive in are miles away from the needs of a life at sea. This is a natural condition shaping our perspective; however, we could realize that, in some case, we are grazed by those needs.

Picture yourself as a businesswoman or man. You need to ship something oversea, let's say container stacks. The shipping could be cheaper or quite expensive depending on your harbor of arrival choice. As you are being forced to choose a particular port, because it's the only within miles that is able to host your huge container ship, you start wondering why the others did not meet the requirements: they seemed vast enough!

It could be a depth issue. Something insiders call bathymetry.

Now pretend to be a tourist, visiting the Italian riviera. You are walking to the beach on a hot summer day. As you get your feet on the sand, you see a local authority telling people that it is not possible to swim. You are forced to walk a long way to reach another beach, miles away. Back to your hotel, having dinner and watching the news, you find out that an algal bloom has been ongoing. Again, after overthinking your bad luck, you start wondering why it is happening on that particular beach only, and not on the other ones.

Perhaps it deals with the shape of sea bottom in that area, something insiders call morphology; and they know it can affect water movements.

In our last example you will be a contractor. You have been given a major inshore work to plan and build. You start approaching the construction site, studying its mechanical and dynamical characteristics. Then, before drawing blueprints you must take measurements, but the area you are dealing with is such a vast one. You create a map with different kinds of measurements, but your sparse points do not characterize the site properly. Just like the previous imaginary people you start wondering, yet again, if there is a faster way providing you with an acceptable level of accuracy.

Here the answer would be a technology that allows you get an instant and wide overview of the site. You could resort indeed to what insiders call remote sensing.

The trivial examples we have seen, are hinting at the current possibility to resort to satellite images and measurements.

An increasing number of professionals is benefiting from this constantly evolving technology. Let us think about geologists, engineering and building operators, search and rescue personnel, safety authorities and environmental agencies. Furthermore, researchers all over the world have the possibility to access a huge, and still growing set of data, images and measurements.

In this work we are going to deeply explore some of the possibilities we are given by satellites and other platforms. Particular attention is given to the bathymetry related aspects, and how we can take advantage of them.

Remote sensing is not a newly conceived discipline. It provides mankind with a whole new perspective of the Earth's surface from the half of XIX century, when early images were taken from kites, messenger pigeons, and unmanned balloons. Obviously, these were just photos and were not used for computations and measurements. Nevertheless, this represented an early, unaware spark for remote sensing inception.

As a matter of fact, the discipline evolved itself over time. A lot of impetus was given by the atrocious occurrence of the World Wars, and, later, by the era of the Cold War. These events had the effect of encouraging research and development, particularly concerning the surveillance technologies and the space exploration. Time became favorable for the launch of a device capable of communicating and collecting information, while orbiting around the planet: the satellite.

Currently we have more than 5,000 active satellites, moving above our heads, collecting images, sending and receiving data.

Before the coming of the satellite, the only way to study remote places such as Antarctica or the ocean, was a scientific campaign. Throughout these missions, hazardous situations and exorbitant costs were considered, in order to collect direct information, otherwise known as in-situ measurements. This traditional approach persists but has been flanked by the remote sensing designated instruments: satellites and planes or drones. These technologies, with their infrastructures and components, allow us to acquire data, sitting at a desk, with one simple click and on an unhoped-for spatial scale. This is clearly notable for the *items of expenditure* of the scientific missions, but first and foremost for the safety of people conducting research activities.

We understand that there is a trade-off between the traditional approach and the contemporary one. We gather in fact that accuracy and precision are involved. The first approach has risks and costs but there is nothing more accurate than a direct value. The latter is safer, less expensive and less time-consuming, but lacks resolution and therefore accuracy. Consider the fact that we are now overlooking the physical difficulties given by a remote sensing activity involving water, such as penetration of the emitted signal, if we are using an active sensor. Nevertheless, we are going to address this later.

We have started scratching the surface of the topic, but here comes the question we are going to carry along, throughout the thesis: is the satellite remote sensing of bathymetry ready? Could the so-called *Satellite Derived Bathymetry (SDB)* compete with the accuracy

given by a traditional approach? If not, what does it take for this technology, to rise as a valuable alternative?

Work presentation

In the current work an algorithm is evaluated. In our case, it is a set of steps allowing us to retrieve bathymetry from satellite imagery. The algorithm we are talking about is an empirical one: the Stumpf algorithm.

The bathymetry retrieval has been carried out in different environments. The first is the Roja river mouth (Imperia, Italy), where single-beam track and aircraft orthophotos were acquired. The second is a coastal marina in Finale Ligure (Savona, Italy), where we have another single-beam survey and a drone orthophoto. Both sites are located in the western Ligurian riviera.

For each site a Sentinel 2 satellite image was chosen, to extract bathymetry using the aforementioned algorithm. The multispectral imagery allowed the ocean-color analysis, necessary requirement for the algorithm. A comparison to the in-situ measurements was carried out to evaluate the process effectiveness.

In the first part of the paper, the theoretical premises are addressed. We talk about satellite infrastructure, sensors, electromagnetic impulses theory, displaying some formulas that helps us keeping it rigorous. This part paves the way for the case studies.

In the second part, practice is dealt with, applying the theoretical methods to the two real datasets. This is the center of the paper, in which we lay the foundation for the conclusion; that is to say the answer for our opening question: can the satellite be a reliable instrument in the bathymetry retrieval?

Theoretical Premises

Hints about satellites

A satellite is a machine moving around the Earth, after being launched into space. The purposes of these pieces of technology are several: they can be used to take pictures for meteorology or safety or for scientific research activities, to communicate for broadcasting or for positioning. Their ability is to be able to collect a larger amount of data and quicker than instruments on the ground. A group of more than twenty satellites makes up the GPS.

Nowadays GPS systems are embedded in a diverse range of technologies we use in everyday life, but what we call GPS is a wider international infrastructure than we think. GPS (Global Positioning System) is just the United States satellite constellation name. It is just a fraction of the vast number of interconnected items which orbit thousands of kilometers above our heads. This network is called GNSS (Global Navigation Satellite System) and encompasses constellations from various countries – including the aforementioned GPS, GLONASS (Russia), Galileo (Europe), BeiDou (China), and IRNSS (India). All these systems are interoperable, provided that no military-related reason prevents their use. The kind of receiver determines which constellation will be used to gather the signal.

The Global Navigation Satellite System is composed of several different segments, namely: orbiting satellites (space segment), system managing stations on the ground (control segment), and receivers (user segment).

Satellites are equipped with atomic clocks, which help determine their location in space. Therefore, any receiver is able to read the electromagnetic signals emitted by one or more satellites. Based on the time information, it can determine its location on the surface of the earth by triangulation.

System managing stations on the ground must monitor the satellite position, making sure that they follow a predefined orbit. When they don't, stations send a message to the satellite, which then actives its thrusters and changes its position accordingly. That's why an artificial satellite can no longer operate when it runs out of fuel. From this moment on, the satellite is labeled as space waste.

Satellite technology is not just resorted to for positioning and long-distance communications. It plays a major role in Earth Observation (EO) too.

EO is a scientific branch gathering several kinds of data. These can be referred to the physical properties of the Earth, its chemical phenomena, or even the biological processes taking place on its surface. The above-mentioned characteristics of satellites, make this technology recommended and progressively more reliable in monitoring the environmental evolution of our planet. This is even more relevant if related to the support that can be given to policymakers. That is why an increasing number of countries and administrations are investing in the creation of databases, were data from a variety of instruments are collected. The main source of data is represented by the remote sensing solutions, as they can constantly provide larger scale overviews of the studied phenomena.

Remote sensing has been a relevant field of study during last decades and keeps branching out as remarkable discipline.

Contemporary satellites are equipped with tools that can perceive and measure several parameters. These tools are referred to as *sensors*. They are capable of detecting usually invisible to the naked eye information, receiving a discrete portion of the electromagnetic spectrum. A sensor can be either passive or active.

The first kind is able to only detect the incoming signal. Reception of different wavelengths, reflected or emitted by any object, determines the production of digital information. For example, solar radiation can reach a sensor after being backscattered by the ocean surface or deflected by the gases composing the atmosphere. Passive sensors are

generally designed to receive spectrum wavelengths in the visible interval and in the infrared one. The foremost disadvantage of equivalent sensors is that they cannot be utilized when favorable meteorological conditions are not met (cloud cover, no solar radiation).

To solve this problem, active sensors are made use of. They are more complex and more expensive. They generate an impulse by themselves and analyze its reflection at a later time. In this case original pulse variations produced by the surrounding irradiated objects are evaluated to create data. The most well-known case in point is represented by the RADAR (RAdio Detection And Raging) technology. It can use low-frequency electromagnetic waves to measure position, distance, or velocity of a target.

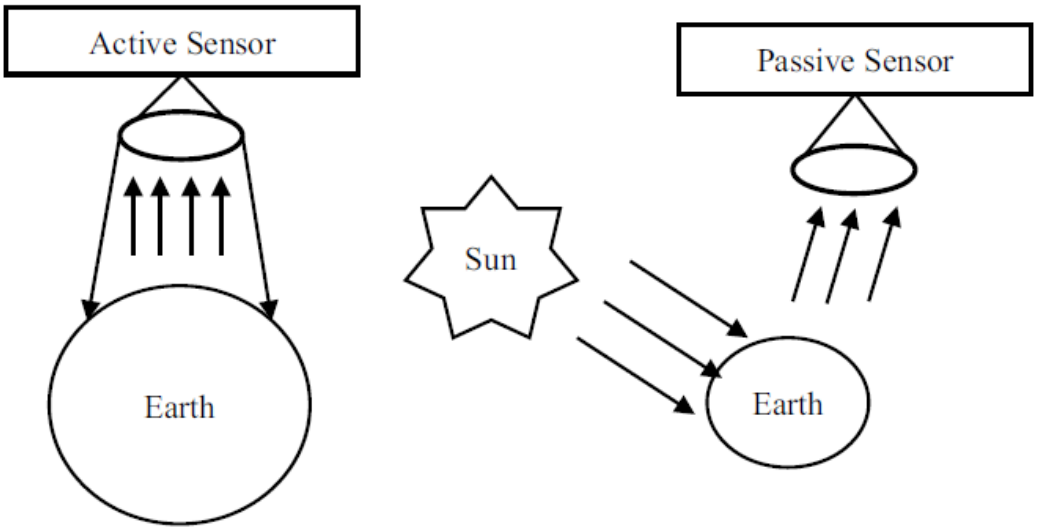

Figure 1 - The concept of active and passive sensors from Satellite Image Analysis: Clustering and Classification - Borra S Thanki R Dey N – 2019

The sensing devices satellites are equipped with, whether they are passive or active, make possible to measure several parameters. Among them some apparently simple instance like distance or other more sophisticated like the strength of gravitational field, and obviously classical physical parameters like temperature and velocity. Collected data can be used to create time series, to build a spatial database for the scientific community or a specific study case, or sometimes they can be merged into models trying to accurately describe the natural phenomena evolution.

Outputs from satellites are not always the same. Their characteristics depend on sensor specifications, on satellite type, on the kind of orbit the satellite is moving in. Orbits are effectively essential to plan a study based on satellite remote sensing. They are variable in altitude, orientation in space, and rotation around the planet. Nevertheless they are defined as stable, meaning a satellite can stay in that orbit for long time. There is a physical explanation: involved quantities, namely gravitational acceleration and centrifugal acceleration, are balanced. Besides, outside the atmosphere, air drag force is equal to zero: an object moves at constant speed. If we assume that the orbit is circular the balanced quantities are going to be expressed as:

$$\frac{\mu}{R^2} = \frac{V^2}{R}$$

(1. 1)

We know μ is given by Earth mass (and satellite mass, here negligible if compared to the Earth's one) multiplying the gravitational constant, R is Earth radius, e V is the normal velocity given by the centrifugal acceleration. We get that required velocity to stay in the orbit is:

$$V = \sqrt{\frac{\mu}{R}}$$

(1. 2)

where R becomes the orbit radius.

We realize that a satellite near the Earth is subject to a larger gravitational acceleration and has to move with velocity equal to the downward force. On the contrary, a satellite orbiting at greater distance can move at lower velocity, since the antagonist force is smaller.

There are different categories of orbits. They can be classified according to their altitude (low, medium, high orbits), to their inclination (equatorial, polar, retrograde orbits), or according to their operative usage (graveyard orbit, parking orbit, commercial orbit).

In our case is useful to describe the orbits that are most commonly used in remote sensing: geostationary orbits and heliosynchronous orbits.

Geostationary orbits are located at 36000 km of altitude above the equator. They are characterized by a revolution period that is equal to the Earth sidereal day. This means a satellite moving in such orbit can have constantly the same overview on the Earth surface. This is given by the fact that satellite movement is tracing over the Earth rotation around its axis. This type of orbit can be referred to as geosynchronous. The advantage in using this sort of track is that we get the same perspective of our planet's surface, within small time intervals. This makes the outputs easily comparable. On the other hand resolution can't be optimal, because of the great distance from the Earth.

Heliosynchronous orbits are characterized by altitude and inclination values, that are set up to have the satellite collect data from different portions of terrestrial surface. Acquired data always have same local solar time too. This is possible thanks to the fact that the Earth rotates around its axis, while the satellite is revolving around the Earth. Every time the satellite makes a complete revolution, a new scanning strip of the surface begins. This is called swath, ranging from tens to hundreds of kilometers in width. The synchronicity with the Sun is fundamental for passive sensors, needing solar radiation, and to have more comparable images: they are collected when the Sun's angle on the horizon is the same, providing same illumination for different surface portions. Generally heliosynchronous orbits are located at 600-800 km in altitude with 95°-100° of inclination on the terrestrial equatorial plane, in fact they are called *near-polar* orbits too. They provide better resolution than geostationary orbits, but revisiting time ranges from some day to tens of days, limiting usability.

We stated that the sensor is the element where the remote sensing happens, that is to say the data acquisition. What then makes it possible for this piece to properly work?

A sensor is nothing more than an electronic circuit, composed by basal units with different complexity degree. Commonly, two parts are to be found: the optical system and the sensor itself.

The optical system is a set of lenses collecting electromagnetic radiation coming from a particular light cone in the space (Ω_S). The cone is defined as the instantaneous field of view (IFOV). Radiation is then conveyed to the Charged-Coupled Device (CCD), a circuit made up by semiconductors that can accumulate an electrical charge proportional to incident radiation intensity. The sensor itself is therefore constituted by a CCD array, in a single line or organized in a grid. The CCD number is proportional to the electromagnetic spectrum bands the sensor can detect (VIS, NIR, SWIR, UV etc.). Being the heart of the sensor, CCDs convert TOA (Top Of Atmosphere) reflectance into TOA radiance, registering its value in digital format on a proper file. Registered values are then merged to compose the output image.

Reflectance, radiance, and other physical concepts are going to be addressed shortly.

Physical background

Let us now turn our attention to the physical foundation of satellite remote sensing, as we are going to focus on the aspects shaping color analysis. Addressing these premises is paramount to pave the way for our work.

As illustrated, the presence of solar radiation is a sine qua non of passive sensors' proper operation. Sunlight propagates in the space, passing different media. These can be the atmosphere, the ocean surface, the water column etc. Each passage entails spectral composition variations of incident radiation. The satellite sensor standing at the end of radiation's path, registers the total amount of aforementioned alterations. As a general rule, a ray of light passes through the atmosphere and later propagates through the water column until it is upward reflected by the seafloor. A part of incident light is reflected at the air-water interface too, determining a partial penetration in the column water. The

final radiation, detected by the sensor, stores all passage variations occurred. We can take advantage of it to study the physical state of encountered elements.

The transition of an electromagnetic wave through an interface between layers with different refraction index (n), is a double phenomenon. It is made up by a reflection event and a refraction event. The physical law deciphering this kind of natural occurrence is the Snell-Descartes law (Huygens, 1690). Their essentials tell us that in reflection the incidence angle is equal to the reflection angle:

$$\theta_i = \theta_{refl}$$

(1. 3)

whereas in refraction we have:

$$\frac{sin\theta_2}{sin\theta_1} = \frac{n_1}{n_2}$$

(1. 4)

where $sin\theta_1$ is the incidence angle and $sin\theta_2$ is the refraction angle. The refraction index (n) is a dimensionless quantity. It depicts the slowdown of an electromagnetic wave passing through a material, given by:

$$n = \frac{c}{v}$$

(1. 5)

where c is the speed of light in vacuum and v is the radiation's phase velocity through the medium.

Previous correlations allow us to appreciate how variable the signal reaching the sensor is, due to the various layers it moves through. Even the atmosphere or the water column can be described as a stack of strata with different density. This is due to multiple factors, like temperature and salinity for water, or temperature and humidity for air masses.

Radiance

Some helpful definitions are going to introduced, and they are important to take more aware steps throughout this work.

The first quantity is radiant energy. It is the total energy emitted by a light source towards the infinite space directions. It is measured in joule (J), therefore we can figure out we are physically dealing with amount of work.

Differently, the radiant flux is the energy flux generated by the above-mentioned source. That is to say the energy that is radiated per unit time. The addition of time in the definition implies we are facing power. As a matter of fact its unit is the watt (W).

Starting from those measures, others can be derived. The physical amounts we can obtain, relate aforementioned quantities with spatial domain. Radiant energy density is the energy amount per unit volume $\left(\frac{J}{m^3}\right)$, yet again radiant flux density is power per unit surface $\left(\frac{W}{m^2}\right)$. Given a radiant flux ϕ intercepted by an area A, the radiant flux density is:

$$E = \frac{\phi}{A}$$

(1. 6)

The flux radiating a surface is called irradiance (E). On the contrary, a flux emitted by a surface is called emittance (M).

If the surface receiving the light is a sphere, the scalar quantity representing the measured light field is named scalar irradiance and written as E_0. The light flux coming from several directions contributes to E_0, which is in fact independent from orientation (that is why we call it scalar).

If the surface receiving the light is a plane, the light radiation is incident to the surface on one side exclusively. In this case the contribution of the light hitting the surface depends on the arrival direction. Planar irradiance is therefore to be related to the spatial orientation of the irradiated surface. This concept is usually applied to oceanography,

because quantifying the irradiance passing through the seawater surface is essential for every remote sensing operation. The ocean surface is generally approximated to a planar surface. The energy flux going deeper in the ocean is called downwelling irradiance, written as E_d, on the other hand the flux reflected from the bottom upward to the surface is called upwelling irradiance, indicated with E_u.

Until now we considered the total amount of the light energy as generated by a single source. However, if we wanted to study its behavior, considering the propagation direction, we would have to introduce the radiant intensity concept. It is the radiant flux, incoming or outcoming, per unit solid angle, expressed in steradian $\left(\frac{W}{sr}\right)$.

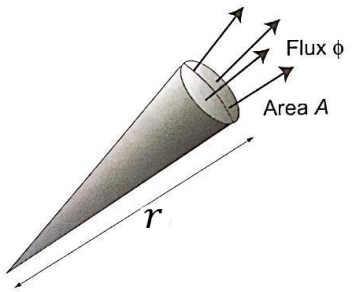

Figure 2 - Solid angle

To clarify: given a sphere, whose center is in the vertex of the angle and the portion of sphere surface intercepted by half lines forming the solid angle Ω; we call A the surface portion, S the whole sphere surface, r the sphere radius.

$$\Omega = \frac{A}{r^2} \tag{1. 7}$$

Because of that, the steradian is a dimensionless unit defining the amplitude of the solid angle. The radiant intensity can be reasonable only if we can consider the source as a punctual one.

Now we are going to introduce a further parameter: radiance. This is a relevant quantity in remote sensing. It is commonly indicated with L, and represents the radiant intensity per unit surface of reprojected source $\left(\frac{W}{sr \cdot m^2}\right)$.

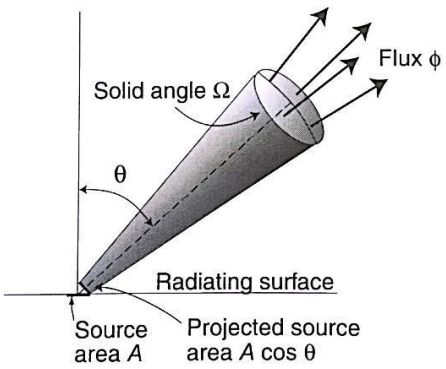

Figure 3 - Solid angle referred to radiance concept

Radiance is a quantity depending on the incoming direction. Given a surface, its radiance varies changing the direction it is observed from. Radiance is useful to quantify light that is detected by an optical system. It is used to evaluate what we could name, with an improper and non-quantitative term, brightness. The word brightness is here used just as an explanatory one, since current scientific lexicon establishes to call radiance what, in everyday life we would call brightness, that is the power of a light source of given surface and seen from a defined angle of observation. We get that this parameter can be helpful considering specifications and employment of satellites.

In the remote sensing's field of interest, the ocean surface is considered an extended light source, as opposed to punctual sources. Additionally, it is thought about as a Lambert surface, in other words an ideal surface reflecting incident energy equally towards each direction. This means that changing the point of view, its radiance does not vary. Hence, in the case of the sea surface radiance only depends on upwelling irradiance; and is given by:

$$L = \frac{E_u}{\pi}$$

(1. 8)

Radiance measurement allows to define the light field of a surface, but that implies to know the directional distribution of the radiation at each point. We get that a parameter

like that is difficult to determine. It is convenient to use an undirect computation starting from relationships with radiance, as follows:

$$E_0 = \int^{4\pi} L \, d\omega$$

(1. 9)

Scalar irradiance: integrating radiance for the whole sphere.

$$E_u = \int^{2\pi} L \cos\theta \, d\omega$$

(1. 10)

Planar irradiance: integrating radiance for the upper hemisphere of the spheric surface approximated to planar.

In addition, let us define a diffuse attenuation coefficient at a point K, at a wavelength λ:

$$K(\lambda) = -E^{-1}(\lambda, z)\frac{dE}{dz}$$

(1. 11)

Where z is the water column depth and E can be whether E_u or E_d, according to the case we are dealing with.

Sometimes the reflectance is used to compute the amount of the downwelling flux that is reflected back to the surface:

$$R = \frac{E_u}{E_d}$$

(1. 12)

For our remote sensing purposes, it is helpful to utilize a ratio between the water-leaving radiance and the downwelling irradiance. This is a hybrid parameter called remote sensing reflectance, and defined as follows:

$$R_{rs} = \frac{L_W}{E_d}$$

(1. 13)

The Table 1 below shows a summary of the parameters previously introduced, as they are the foundation of passive remote sensing.

Physical quantity	***Formula***	***Symbology***	***Unit of measurement***
Radiant energy	//	Q	J
Radiant flux	$\frac{\mathrm{dQ}}{\mathrm{dt}}$	ϕ	W
Radiant energy density	$\frac{\mathrm{dQ}}{\mathrm{dV}}$	W	$\left(\frac{J}{m^3}\right)$
Radiant flux density	$\frac{\mathrm{d}\phi}{\mathrm{dA}}$	E (incoming*) M (outgoing*) *in reference to the surface	$\left(\frac{W}{m^2}\right)$
Radiant intensity	$\frac{\mathrm{d}\phi}{\mathrm{d}\omega}$	I	$\left(\frac{W}{sr}\right)$
Radiance	$\frac{\mathrm{dI}}{\mathrm{d(Acos}\theta)}$	L	$\left(\frac{W}{sr \cdot m^2}\right)$

Table 1 - Summary of physical quantities commonly used in ocean color remote sensing

Sensor measurements

The sensor that is installed on satellites is, for all intents and purposes, a radiometer. This means it is suited to measure the flux of electromagnetic radiation emitted by a surface, namely the surface's radiance.

Geometric properties of the sensor in VIS or NIR bands, are given by a lens array that coveys light coming from a particular directional cone (Ω_s) into the sensor. This defines the Instantaneous Field Of View (IFOV). Considering a small sea surface dA, included into the IFOV of the sensor with aperture A_s, a distance from the surface R_s, a referred to the normal sensor inclination θ, if radiance in the direction θ is L, then from radiance's definition we have that the radiant flux from the surface dA that is intercepted by the sensor is:

$$d\phi_s = L\cos\theta\frac{A_s}{R_s^2}dA$$

(1. 14)

where $\frac{A_s}{R_s^2}$ is the solid angle subtended by sensor aperture.

In order to obtain the total flux of the area A included in the sensor IFOV, we have to integrate previous equation on the whole surface we are considering, getting that:

$$\Phi_s = LA\cos\theta\frac{A_s}{R_s^2}$$

(1. 15)

Determining A from IFOV's definition we have:

$$A = \frac{\Omega sRs2}{cos\theta}$$

(1. 16)

obtaining so:

$$\Phi_s = LA_s\Omega_s$$

(1. 17)

Since A_s and Ω_s are both fixed sensor properties, the picked-up signal is directly proportional to the surface's radiance and independent from view angle θ and surface-sensor distance.

Now let us consider the spectral characteristics of the sensor in the visible band. The tool is designed to capture light waves in a band ranging from λ_1 to λ_2, measuring for this reason:

$$\phi(\lambda_1 \rightarrow \lambda_2) = \int_{\lambda_1}^{\lambda_2} \phi_\lambda \, d\lambda$$

(1. 18)

To avoid unwanted and unrelated contributions, band-pass filters are commonly utilized. Filters like these can attenuate radiations coming from outside the band range we are interested in. The sensor output S is therefore a combination of radiometer's feedback and filter's response $R_f(\lambda)$:

$$S = \int_0^{\infty} \phi_\lambda R_f(\lambda) \, d\lambda$$

(1. 19)

To study phenomena characterized by high spectral variability, a finer band subdivision is required. The only problem is that we have to able deal with such a finer-grained resolution.

Atmosphere optical features

Let us now examine the media an electromagnetic signal propagates through. Solar radiation enters the atmosphere, goes on into the water column, and reaches the sensor again through the atmosphere. During this miscellaneous path, some information is lost and some other is taken on. It is important to distinguish between signal of interest and interferences. This is done taking advantage of a classification of light rays, based on following categories.

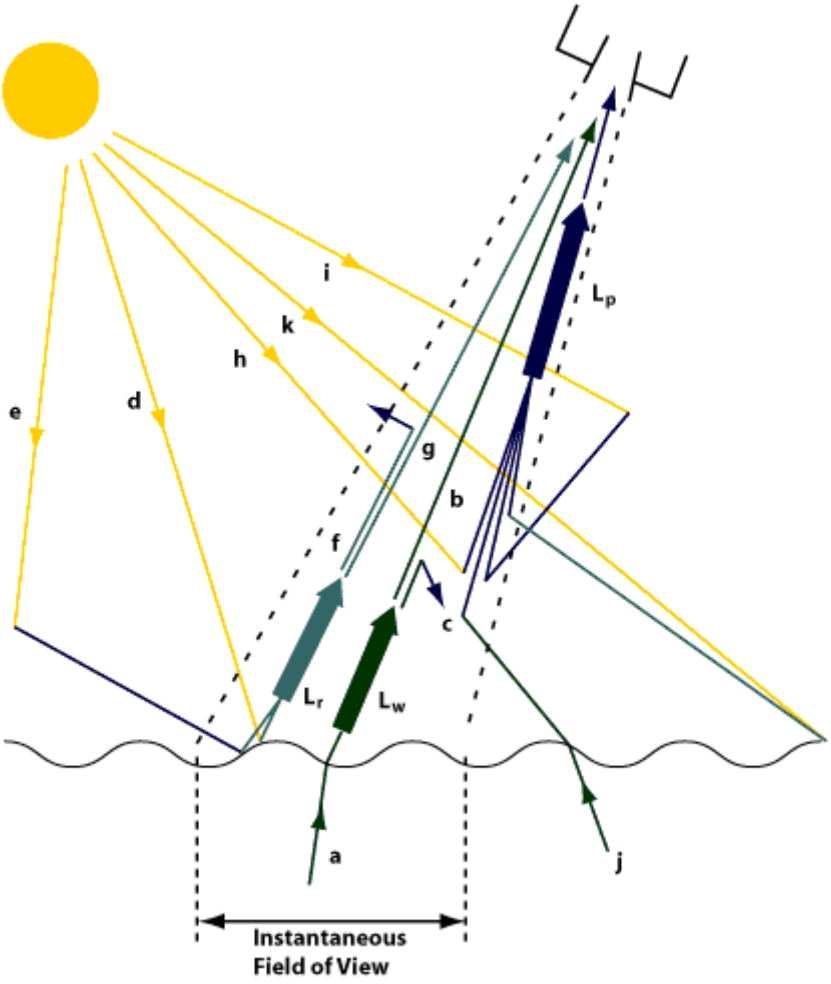

Figure 4 - Illustration of several different light pathways in the atmosphere from Satellite Observations of Ocean Colour, Philosophical Transactions of the Royal Society of London Series A - Robinson

- The first light rays we discuss about, are those rays passing through the atmosphere, penetrating water column, being reflected back at a certain depth, and concluding their pathway to the sensor staying within the IFOV. These rays make up the *water-leaving radiance* L_w. Rays composing L_w can have different behavior: either reaching the sensor (see letter b in Figure 4) or leaving the IFOV because of atmospheric disturbance (c).
- Rays being reflected into the IFOV, by water surface or by atmospheric layer's refraction, are called respectively *sun glitter* and *sky glitter*. Their total contribution is the radiance only due to ocean surface reflection L_r. As in the prior case, a part of radiation is then lost because of interferences (f), the residual part is detected by the

sensor (g). This generally determines a twinkling effect to be seen in the output imagery, and to be corrected during postprocessing.

- Otherwise, there are rays that are refracted by the atmosphere towards the sensor (h).
- Rays reflected by a part of the ocean surface outward the IFOV, but then refracted back into the IFOV by the atmosphere (j).
- Rays propagating through the water column up to the ocean surface, where they leave the IFOV to be then refracted back into the IFOV. This last class is commonly indicated as L_p, or rather the contribution of the radiance due to light transmission within atmosphere (i,k,h).

Summarizing what has been stated, the total computation of above-mentioned components constitutes the incoming radiance at the sensor L_s:

$$L_s = L_p + TL_w + TL_r \tag{1. 20}$$

where T is direct transmittance of atmosphere, a factor indicating the portion of radiance leaving the ocean surface and not being deflected out of the IFOV.

State of the art of SDB

Technologies have evolved in the last decades. Remote sensing has been branching out in the private sector as in the public one. New instruments have given strength to this multi-purpose discipline. Though a final single technology is not ready yet, currently we can count on many valid alternatives in the study of bathymetry.

Remote seafloor mapping is nowadays feasible through a wide range of options, such as satellites, unmanned aerial vehicles (UAVs), planes, Light Detection And Ranging (LiDAR), orthophotos and RAdio Detection And Ranging (RADAR).

The first significant issue to be addressed, is resolution. Many authors agree upon the importance of having high spatial resolution (Dayem & Akter, 2020; Lyzenga et al., 2006; Monteys et al., 2015; Salavitabar et al., 2022; Stumpf et al., 2003).

Because of this, a growing amount of works are carried out relying on commercial satellites imagery, such as IKONOS (Lyzenga et al., 2006), QuickBird (Stumpf et al., 2003) and World View-3 (Niroumand-Jadidi et al., 2020; Salavitabar et al., 2022). These platforms made available imagery with pixel dimensions of 4 m or better. However, there is an important part of the scientific community that tends to adopt open solutions just like Landsat 8 from NASA and USGS, or like the European Space Agency's Sentinel-2. (Dayem & Akter, 2020; Wei et al., 2021).

We figure out that resolution can play a major role. This is factual when our purpose is to detect bathymetry, and when we want to perform a habitat mapping as well. Actually, we know these fields of research are connected: depth knowledge and bottom albedo detection can give an advantage in improving habitat classification (Mumby et al., 1998).

Technologies representing the so-called non-imaging part of remote sensing, measure actively the distance between the sensor and the water surface/sea floor. LiDAR, for instance, is widely used but, in some cases, it is not the optimal solution. This instrument can reach 4 m resolution horizontally and 20 cm vertically, at depth of over 30 m. However, it is not ideal for all water types. Satellite LiDAR are not able to provide high-accuracy bathymetric surveys, as they are not designed for that specific purpose (Coveney & Monteys, 2011; Monteys et al., 2015).

On the other hand, imaging methods base the estimation of water depth on the pixel values of an image, acquired by passive sensors. In the last decades, airborne optical sensing of bathymetry has been the most frequently used for a wide range of water bodies,

including inland lakes, shallow estuaries, coastal areas, and open seas. This method has been implemented either analytically or empirically, starting from Lyzenga in 1985 till its affirmation due to the GNSS advent (Gao, 2009).

In more recent years, the easier commercialization of UAVs has given a boost to their usage in remote sensing research activities. They are small and light, usually equipped with a GNSS system and a multispectral camera. Furthermore, they represent an alternative to the more expensive usage of airplanes, and they can provide few centimeters of spatial resolution, because of the reduced viewing distance achievable.

Optical sensors employed in research are various. Namely multispectral, superspectral, hyperspectral. They are classified according to another kind of resolution: spectral resolution. Multispectral sensors have a smaller spectral resolution, that is to say 9 or 10 bands. In the case of hyperspectral ones, more than 16 bands can be reached. Multispectral images are commonly used, defining a few intervals in the VISible spectrum and Near Infrared one.

We see how the performances of the sensor involved in imaging remote sensing, are variable. They change according to the platform they are attached to. It could be a satellite, an airplane or an UAVs.

Their results are affected by a variety of conditions. Satellites, for instance, cannot work if cloud cover is present. Satellites and airborne derived bathymetry are both strongly influenced by turbidity. Water turbidity and color are in fact one of the factors affecting light levels in water, along with water-surface backscatter and substrate reflectance (Winterbottom & Gilvear, 1997).

An expeditious evaluation for turbidity using a Secchi disk is commonly performed, when using a drone or a plane. The depth at which the disk is no more visible is called Secchi-depth (here indicated with ε). For LiDAR maximum reachable depth is equal to 2ε if a high-frequency sensor is used, and 4ε for a low-frequency one (Pizzeghello & Sinapi, 2022). Turbidity can have many concurrent causes, for example pollutants or sediments

due to rain run-off and river supply. The remote sensing algorithms response is different and depending on the site characteristics. Although passive optical systems are limited in depth penetration and constrained by water turbidity, the use of such data might be the only viable way to characterize either extensive or remote environments, like for instance coral reefs (Stumpf et al., 2003).

Concerning water-surface backscatter, wind can play a relevant role. If the sea surface is too smooth, we get a kind of mirror effect called *sun glint*. An effect we have to correct during the pre-processing phase. On the contrary if the water surface is too rough, light is not able to penetrate properly. Sea state is therefore something to be accounted for.

The state of the art in bathymetry measurement is still represented by the MultiBeam EchoSounder (MBES). No other instrument can provide the accuracy and the information of this instrument. The SingleBeam EchoSounder is accurate, nevertheless its spatial resolution is often not adequate to interpolate between the strips of acquisition.

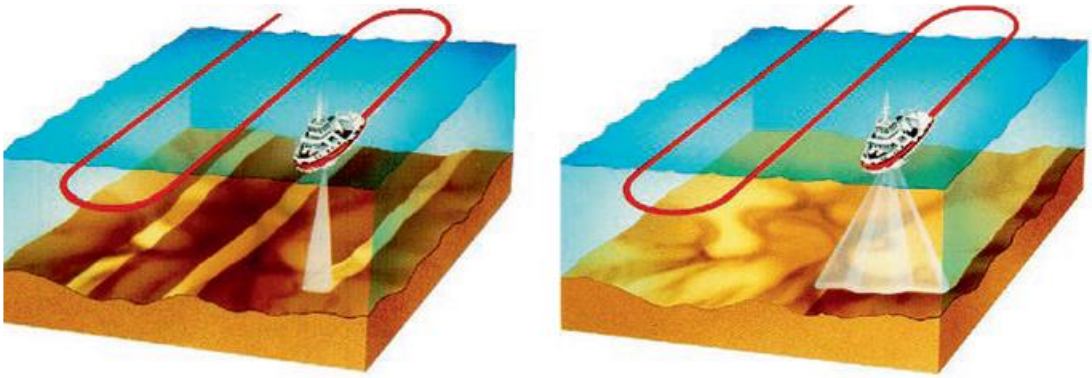

Figure 5 - Difference between singlebeam and multibeam survey (courtesy of Kongsberg Maritime AS) from *Measurement for the Sea Supporting the Marine Environment and the Blue Economy – Springer - 2022*

The MBES is the traditional instrument used to measure the depth below a transducer, transforming electrical energy into acoustics in transmission and vice versa in reception. An acoustic impulse at a certain frequency is emitted at a known time, and the return signal time is measured. Known the profile of the speed of sound in the water, the distance from the transducer to the seabed is calculated by measuring the travel time. The result is

a precise measurement of the depth over time, taking advantage of the fact that the vehicle on which the instrument is installed is moving along programmed lines. In order to intercept the depth variation profile on each acquisition line, the lines are generally conducted perpendicularly to the average bathymetric trend of the surveyed area (Pizzeghello & Sinapi, 2022).

MBES is the instrument to choose when surveying areas where high accuracy is needed: harbors or any area with minimum underkeel clearance. Besides MBES and SBES can be used as in-situ measurement to calibrate other retrieval techniques. LiDAR can be used too: where depth is not great, airborne measurements can be used as ground truth occasionally. However, non-satellite remote sensing data sources based on aircraft measurement or ground measurement have a higher cost and are limited by their weak capacity for comprehensive observation of large areas of lakes and rivers (Yang et al., 2022). Summing up, we should always use MBES or SBES if we are looking for accuracy but accounting for high economic costs and time-consumption. We can rely on satellites when favoring quickness and synoptic view. Airborne and UAVs technologies (LiDAR or passive multispectral imagery) are compromise solutions to be modeled on the faced conditions and timing.

What has been stated until now for coastal waters, is generally even more valid for rivers. Their nature takes the problem to a whole new level. The irregularity of their beds, the many materials these are made of, the thoroughly variable water flux, need to be addressed with even better detection capacity. In those cases, a detailed preliminary study about the river features is needed (Legleiter et al., 2009).

Nevertheless, how can we discern if the technology we have is suitable for our case of study? The International Hydrographic Office (IHO) established different survey orders in its publication S-44 (IHO, 2020). These are standard rules to provide an official general classification of hydrographic surveys. Rules like these allow measurements to be representative and associated to a certain quality level. This is remarkable from different viewpoints, such as collecting, sharing and using data.

The Table 2 represents the different orders individuated by IHO.

Criteria	Order 2	Order 1b	Order 1a	Special Order	Exclusive Order
Area description (Generally)	Areas where a general description of the sea floor is considered adequate.	Areas where underkeel clearance is not considered to be an issue for the type of surface shipping expected to transit the area.	Areas where underkeel clearance is considered not to be critical but features of concern to surface shipping may exist.	Areas where underkeel clearance is critical	Areas where there is strict minimum underkeel clearance and manoeuvrability criteria
Depth THU [m] + [% of Depth]	20 m + 10% of depth *Ba5, Bb2	5 m + 5% of depth *Ba8, Bb3	5 m + 5% of depth *Ba8, Bb3	2 m *Ba9	1 m *Ba10
Depth TVU (a) [m] and (b)	a = 1.0 m b = 0.023 *Bc7, Bd4	a = 0.5 m b = 0.013 *Bc8, Bd6	a = 0.5 m b = 0.013 *Bc8, Bd6	a = 0.25 m b = 0.0075 *Bc10, Bd8	a = 0.15 m b = 0.0075 *Bc12, Bd8
Feature Detection [m] or [% of Depth]	Not Specified	Not Specified	Cubic features > 2 m, in depths down to 40 m; 10% of depth beyond 40 m *Be5, Bf3 beyond 40m	Cubic features > 1 m *Be6	Cubic features > 0.5 m *Be9
Feature Search [%]	Recommended but Not Required	Recommended but Not Required	100% *Bg9	100% *Bg9	200% *Bg12
Bathymetric Coverage [%]	5% *Bh3	5% *Bh3	≤ 100% *≤ Bh9	100% *Bh9	200% *Bh12
		September 2020			Edition 6.0.0

Table 2 - Minimum Bathymetry Standards for Safety of Navigation Hydrographic Surveys, all uncertainties at 95% confidence level – S-44, IHO, 2020

In this table *THU* and *TVU* stand respectively for *total horizontal uncertainty* and *total vertical uncertainty*. These are propagated uncertainty measurements given by the contribution of the uncertainties characterizing each instrument involved in the process, such as MBES or SBES, GNSS systems, Motion Sensor Units etc. One for the vertical dimension and the other for the horizontal one. Where *Bathymetry Coverage* and Feature *Search* exceed 100%, detection overlapping is requested. Just to give an example with an Airborne LiDAR the maximum achievable order is *Order 1B*, and a direct MBES survey is the only way to achieve an *Exclusive Order*. The standards are published by international organisms, but national authorities are allowed to integrate or give more restrictive indications.

SDB Algorithms

Linear approach

Several algorithms for SDB have been proposed over the past 50 years, based on dissimilar approaches. Some of them are called analytical algorithms, as their foundations are laid by physical quantities. They identify the parameters involved in the insight of a particular phenomenon, in order to establish their relationships and rule them. An example of this kind of approach is the Lyzenga algorithm (Lyzenga, 1978). It is a revision of previous attempts in the analytical retrieval of bathymetry field (Polcyn et al., 1970), among the others one from Lyzenga himself (Wezernak & Lyzenga, 1975). The algorithm designed in 1975 consists of a linear equation in which the author takes into account the physical components giving the radiance value of the *i* band:

$$L_i = L_{si} + k_i r_{Bi} \exp(-K_i f z)$$

(1. 21)

Where L_{si} is the radiance observed over deep water; k_i is a constant including solar irradiance, atmospheric and water surface transmittance, and radiance reduction due to refraction at the water surface; r_{Bi} is the bottom reflectance; K_i is the water attenuation coefficient and f is a geometric factor to account for the pathlength through the water. This equation can be solved for z , which stands for depth. Despite the physical strength of this linear approach, it has strong dependence from the seabed albedo. This should be taken into account where sediments are, so to say, patchy. Where we find heterogeneity in the sediments composing the sea bottom, the reflectance will change just because of the material optical response. This will happen at equal depth, however providing a different radiance value and producing inaccuracy of the output.

The method introduced by Polcyn and refined in linear form by Lyzenga in 1978 consists of a *band ratio*. As a matter of fact we can take advantage of different spectral bands to

overcame the problem given by heterogeneity of the bottom. The algorithm *relies on the assumption that a pair of wavelength bands can be found such that the ratio of the bottom reflectances is the same for all bottom types within a given scene* (Lyzenga, 1978). For bottom types A,B,… we have:

$$\frac{r_{A_1}}{r_{A_2}} = \frac{r_{B_1}}{r_{B_2}} = R_{b_n}$$

(1. 22)

where r_{A_1} is the reflectance of bottom type A in band 1 etc.

In search of a more stable linear method Lyzenga was able to write a general formula of the algorithm, using two bands to correct the bottom material differences:

$$Z = a_0 + a_i X_i + a_j X_j$$

(1. 23)

where a_0, a_i, a_j are constants given by multiple regressions and where:

$$X_i = \ln (L_i - L_{si})$$

(1. 24)

This is a linear method using two bands to account for bottom variations. To use this algorithm 5 variables are to be defined: $L_{si}, L_{sj}, a_0, a_i, a_j$. This can be difficult when dealing with wide study areas. Furthermore, if the area is interested by the presence of macroalgae or *Posidonia oceanica* meadows, L_i is going to be smaller than L_{si} making X_i not defined. This last occurrence jeopardizes the possibility to retrieve bathymetry in the interested zones. We understand that *the disadvantage of this algorithm is to be more complex and therefore more difficult to implement than the ratio methods* (Lyzenga, 1978).

Ratio algorithm

The flip side of the coin is here represented by those approaches involving the ratio between more spectral bands. This *allows separation of variations in depth from variations in bottom albedo* (Stumpf et al., 2003). Furthermore, passive sensors are used to retrieve bathymetry when the investigation is intended to be expeditious. This makes the algorithm that is quicker to calibrate and easier to compute, the best choice.

The Stumpf band ratio method is based on the fact that spectral bands have different absorption degree. This allows us to resort to a ratio between bands to linearize their decreasing with depth radiance value. This is verified even if bottom albedo variations are to be found, since both bands will be affected from seabed optical properties changes, *suggesting that different bottom albedos at a constant depth will still have the same ratio* and therefore *the ratio would approximate depth independently of bottom albedo* (Stumpf et al., 2003). The ratio method we are dealing with, is here represented in its formula, saying depth is equal to:

$$Z = m_1 \frac{\ln(nR_w(\lambda_i))}{\ln(nR_w(\lambda_j))} - m_0$$

(1. 25)

where R_w is the radiance value we get in the two bands λ_i and λ_j; n is just an arbitrary number to assure the involved in the ratio quantities are not negative; $m_1$and m_0 are *tunable constants* that are defined in the calibration process. Generally, the ratio is used as blue band over green band, or blue band over red band where depths are small; furthermore some research suggests summing the bands (Blue/Green + Blue/Red) to get better results(Wei et al., 2021). We see that this method fulfills the aforementioned requirements, being simple in its parameters retrieval. This approach has its own advantages: *it does not require subtraction of dark water, which expands the number of benthic habitats over which it can be applied* and *has fewer empirical coefficients required for the solution, which makes the method easier to use and more stable over broader geographic areas*. On the other

hand, *the ratio transform has limitations relative to the linear transform, particularly in an increased level of noise* (Stumpf et al., 2003). The two approaches seem to give different results according to region chosen and imagery used (Casal et al., 2019; Dayem & Akter, 2020). Another issue affecting both linear and ratio methods is turbidity, that influences satellite sensors performance at first. Anyway, the ratio model seems to perform *slightly better in scattering turbidity than the linear transform* (Stumpf et al., 2003). The ratio algorithm can be calibrated using available in-situ measurements. Empirical algorithms are used, among the others, by Hydrographic Offices of many countries to perform an expeditious assessment of nautical charts adequacy, to plan potential upgrades (Pe'eri et al., 2014).

The Sentinel-2 mission

The Sentinel-2 mission is part of the European project Copernicus. Copernicus is a program, giving the European Union Earth observation capacity, managed by the member states (through the European Commission) and implemented by the European Space Agency (ESA). Sentinel-2 is the second mission after Sentinel-1 and has paved the way for the third mission, Sentinel-3, launched in 2016. The Sentinel-2 mission is composed by a two-satellite constellation placed in a sun-synchronous orbit at 786 km altitude, providing high spatial resolution. The purpose is to *monitor the variability in land surface conditions* (European Space Agency Site, 2022) and this has countless declinations. The sectors in which advantages are taken are for instance: agriculture, forests management, inland and coastal water quality monitoring, disasters mapping and civil security.

The satellites composing the mission were named 2-A and 2-B. The first was launched in 2015 on June 23rd and the latter two years later, on June 7th. Revisiting time is 10 days at the same viewing angle. In some cases, we can have less revisiting time but due to the swath overlap, providing images with different viewing angles. To have more frequent revisits satellites 2-A and 2-B are phased 180° from each other. This makes possible to complete

the 10 days revisiting time in just 5 days. The coverage is global and ranges from 56° S to 84° N for land surfaces.

Each collected data is openly accessible, exploitable, editable. Datasets can be browsed on the online open platform https://schihub.copernicus.eu/. In addition to the satellite imagery online database, multiple services were activated depending on three areas: CLMS (Copernicus Land Monitoring Service), CMEMS (Copernicus Marine Environment Monitoring Service), and CEMS (Copernicus Emergency Management Service). These services are to be reached at https://www.copernicus.eu/en/copernicus-services/ .

Used Software

Geographic information systems are tools capable of managing, processing, and visualizing geo-referenced data. These can be proprietary software like ArcGIS from ESRI™, or open source one, the case of the computer program we used: QGIS, in its 3.22.13 version (QGIS Białowieża LTR) (QGIS Development Team). This kind of software allows us to manage vector and raster data, computing and processing their relationships. As a matter of fact, we used QGIS to prepare datasets for calibration and validation processes. The graphical results like maps are a QGIS output too.

To calibrate and validate data, a MATLAB script was used. The MATLAB version is R2022b. This is proprietary software copyrighted by MathWorks™(The Mathworks Inc., 2022). A student license was provided by the Genova University. Graphical outputs like diagrams have been realized in MATLAB.

Another tool we used is SNAP, in its version 9.0.0. This is an open-source project from ESA, allowing us to preprocess satellite imagery (ESA). In our case we used it to get Sentinel-2 images ready for spatial analysis in QGIS.

Links to software's web pages can be found in the bibliography.

Case Studies

Let us consider now the main features of the here proposed case study. The work is structured over different areas of interest. It involves a various set of instruments, both for the initial surveys and for the later remote sensing implementation. These concurrent aspects are here presented.

Area Description

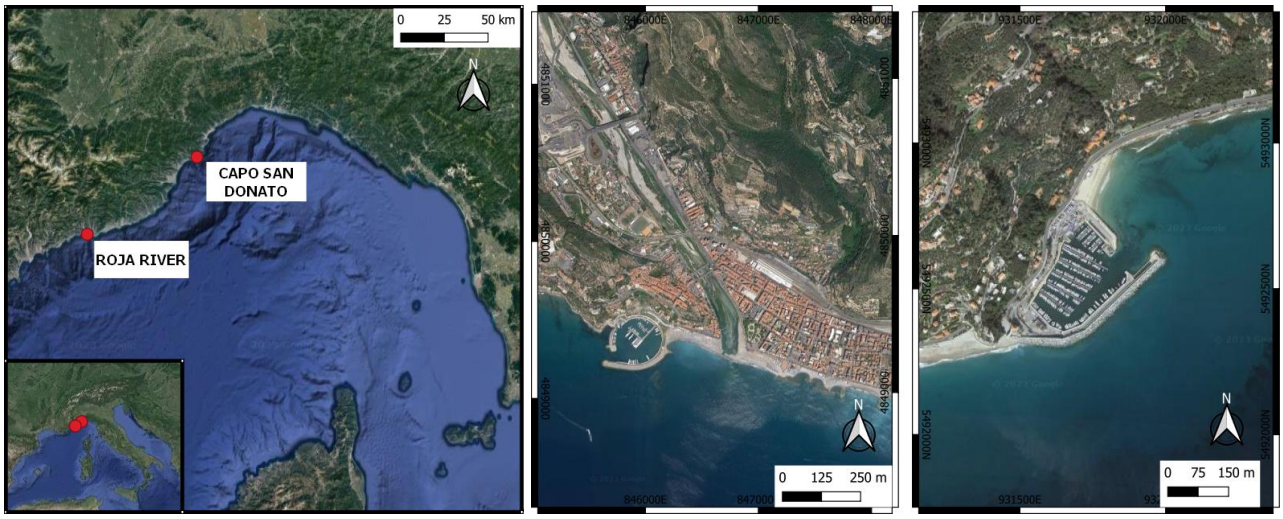

Figure 6 - Overview of the studied areas

The examined case studies relate to two areas in the Liguria region, a narrow land portion fitted between the sea and a mountain range, composed by the encounter of the Alps with the Apennines. This setting is the premise for a complex situation. Available space is not sufficient for the variable density of population. While the coast is overcrowded, the backcountry goes through depopulation. This in need of care territory is therefore either overused or abandoned. Population density is variable spatially as temporally: seasonal tourism is a fact. The summer increase of residing people brings local outdated infrastructures to their knees. In addition, the weather plays a central role in the seasonality of this area. Heavy localized rainfalls and storm surges are just some examples giving the idea of this territory's fragility. Hydrogeological instability is a fact too. This is a

region where extreme events related to anthropogenic changes have had the greatest number of negative effects.

The areas involved in our effort are located in the western part of Ligurian riviera. We are dealing with two different sites: the first is in Ventimiglia and the latter is pinpointed in Finale Ligure. They show different characteristics, since one is a river mouth area, and the other is a coastal one.

For both sites no classification of the substrate is performed, as the bottom is considered as homogeneous.

Roja river

The first site we are going to describe is located in Ventimiglia, a town in the provincial administration of Imperia, Liguria, Italy. The zone we are interested in is to be found at the mouth of the river dividing the center of Ventimiglia, the Roja river. This river is not far from the Italy-France border. Its source is located in the Ligurian Alps, and it runs southward flowing into the Ligurian sea in the area of Ventimiglia city. It is 59 km long and a has an average discharge of 15 m^3/s. Its hydrographic basin is one of the largest within the Ligurian territory, as showed in the picture below.

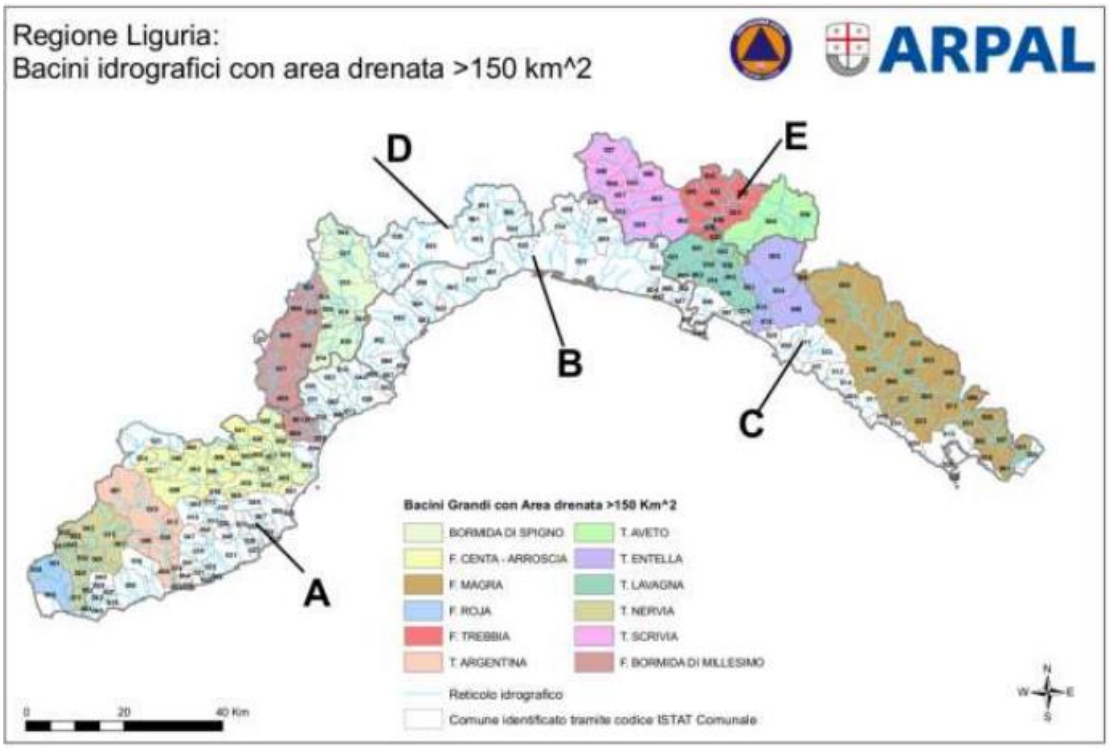

Figure 7 - Ligurian hydrographic basins larger than 150 km², Roja's basin is indicated with sky blue color at left. (Regione Liguria, 2020)

Actually, a previous survey (with its output dataset) has been used for our purposes. This is a survey commissioned by GTER s.r.l. Company, that took place in the river. The work was committed from Regional Institutions to provide an assessment of the river state, as well as an estimation of the river capacity in case of heavy rains to prevent floodings. For the part of the bathymetric data acquisition campaign focusing on the mouth of the Roja river, a shallow water depth was found (from a few tens of centimeters to 4 meters about) and relatively calm state with no evidence of currents that could make difficult acquiring data. (Bibuli et al., 2021)

Figure 8 - Overview of Ventimiglia - ©2003 TerraMetrics

Finale Ligure

The other site we are going to describe is located in Finale Ligure, a town in the provincial administration of Savona, Liguria, Italy. The zone we are interested in is to be found in the eastern part of the town where a marina was built in 1964 and then progressively renovated. Its name is Capo San Donato marina. The depth range is here 0 to 7 m.

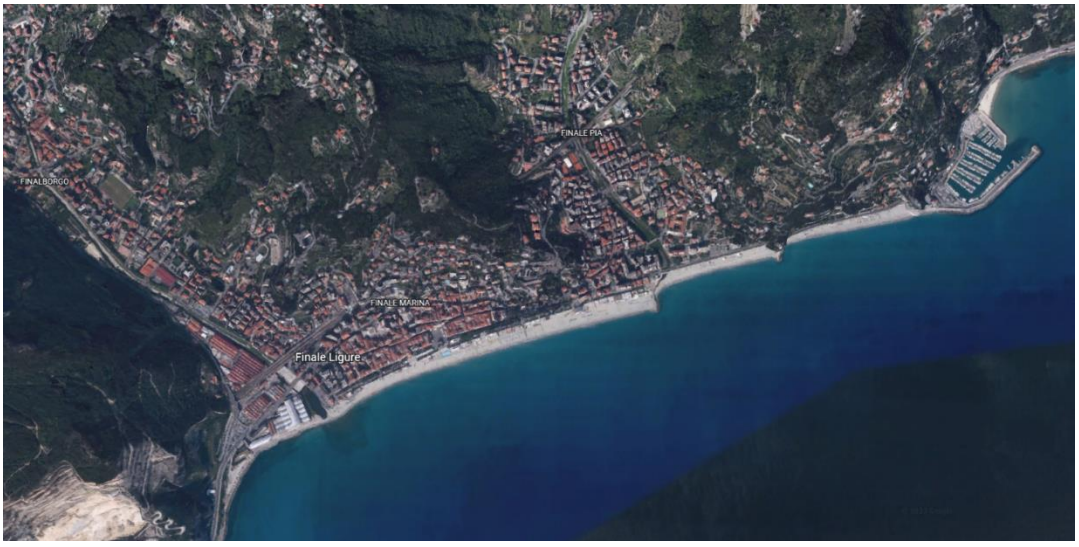

Figure 9 - Overview of Finale Ligure - ©2003 TerraMetrics

Instruments and Technologies

The instruments used during the project are different, in design and purpose. There is a preliminary phase, in which some tool is utilized to create a first dataset. After those passages, other technologies are used to work on and with the initial acquired data. The tools we have relied on preparing this research, are here presented.

SBES surveys

Roja river

In the Roja river area, a single beam echosounder was used to acquire bathymetry. These data are the in-situ measurements for the very zone of the mouth of the river. The employed instrument is actually an Autonomous Surface Vehicle (ASV), particularly convenient when dealing with shallow water, because of its high manoeuvrability and great accuracy. The used instrument is an ASV referred to as SWAMP (to be seen in the picture below). The SWAMP is a full-electric Catamaran that is 1.23 m long with a breadth of 1.1 m. The hull height is 0.4 m and the vehicle with the structure and the antennas is 1.1 m high. SWAMP lightweight is 38 kg with a draft of 0.1 m, the standard maximum payload is 20 kg with a consequent maximum design draft of 0.14 m but the reserve of buoyancy of SWAMP allows to embark up to 60 kg with a draft of 0.22 m. The small dimensions of the vehicle comply with the idea of a reduced logistics. The vehicle is man-portable and transportable by car or in a small boat. A double ended hull was studied for hosting four Pump-Jet Module azimuth thrusters expressly designed and studied for the SWAMP project. The basic Navigation Guidance and Control (NGC) package of each hull is composed by an IMU and a GPS. The communication is created by one 2.4 GHz Wi-Fi communication module. Maximum speed of SWAMP in infinite depth waters is 1.6 m/s, while the speed in extremely shallow waters down to 200 mm (i.e. 60 mm of under-keel

water) is reduced to 1 m/s due to the change in hydrodynamic characteristics occurring in shallow waters. For the Roja survey the SWAMP was equipped with a Microstrain 3DM-GX3-35 GPS + AHRS (attitude heading reference system), and an Echologger ECS400 Single-beam Sonar (working frequency 200 kHz) for river-bottom range measurement. (Bibuli et al., 2021).

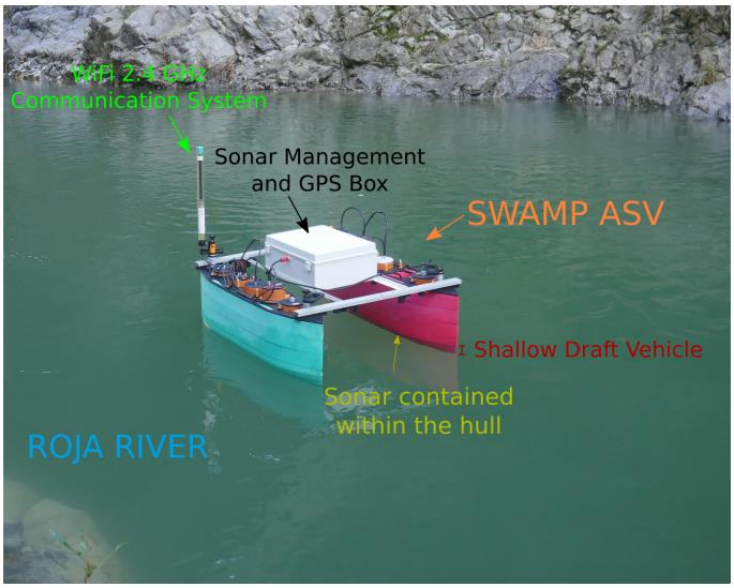

Figure 10 - SWAMP-ASV during the Roja River survey - (Bibuli et al., 2021)

Finale Ligure

In the case of Capo San Donato, bathymetry direct measurement was performed by Maifredi Geological Associated Studio using a Garmin GPSmap 188 Sounder equipped with a double-frequency transducer (50/200 kHz). This instrument provides an accuracy better than 2 m, thanks to WAAS-EGNOS system. The echosounder was associated to a GNSS system Leica GS10, that has few cm accuracy. The survey is made up by orthogonal and parallel strips, referring to the touristic harbor entrance line. Any additional information can be provided by Maifredi Associated Studio.

AGEA aerial imagery

As aerial imagery for the Roja river we used snapshots coming from a campaign by RTI CGR S.p.A / e-Geos S.p.A on behalf of AGEA (Agenzia per le Erogazioni in Agricoltura) within a project named "Accordo Quadro per servizi di telerilevamento funzionali al Sistema Integrato di Gestione e Controllo e di ulteriori servizi di telerilevamento ed elaborazione cartografica per il triennio 2018-2020". That work consisted in orthorectified and georeferenced photogrammetric images taken at 3400 m flying height, over the whole territory of Liguria region ("Ortofoto digitali a colori AGEA 2019"), and in compliance with the guidelines from CISIS (Centro Interregionale per I Sistemi Informatici Geografici e Statistici). The used instrument provided us with a color depth of 32 bit and a spatial resolution of 20 cm. Scale is 1:5000.

Sentinel-2

Both for Roja river case and for the harbor in Finale Ligure, the satellite imagery was downloaded from the official platform for retrieving Sentinel-2 data. Images were already preprocessed by the platform. A presentation of parameters characterizing this satellite mission follows.

Sentinel-2 satellites systematically acquire optical imagery taking advantage of 13 different spectral bands at different spatial resolution, ranging from 60 m up to 10 m. This means the perspective of the Earth surface we get from this kind of products is a discretized one: the surface is composed by 10 x 10 m pixels, at best.

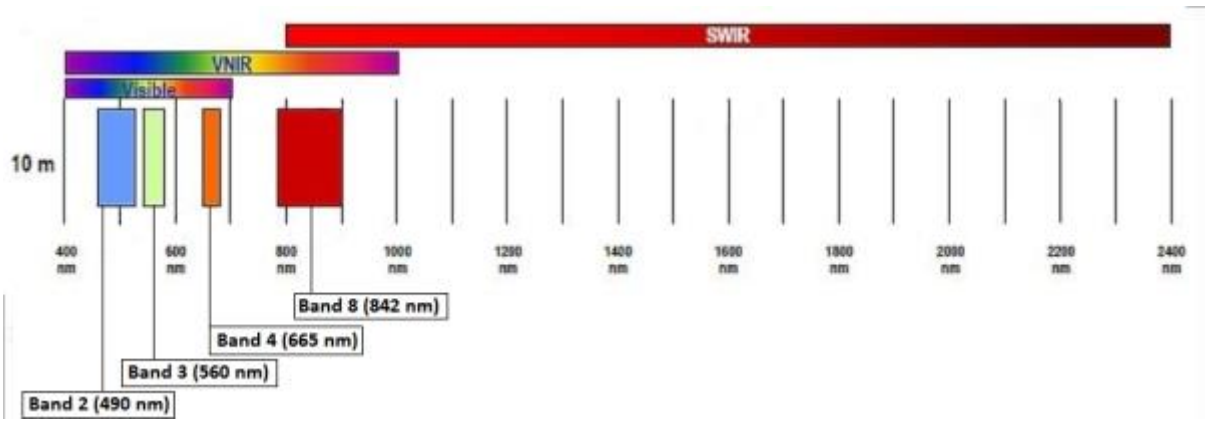

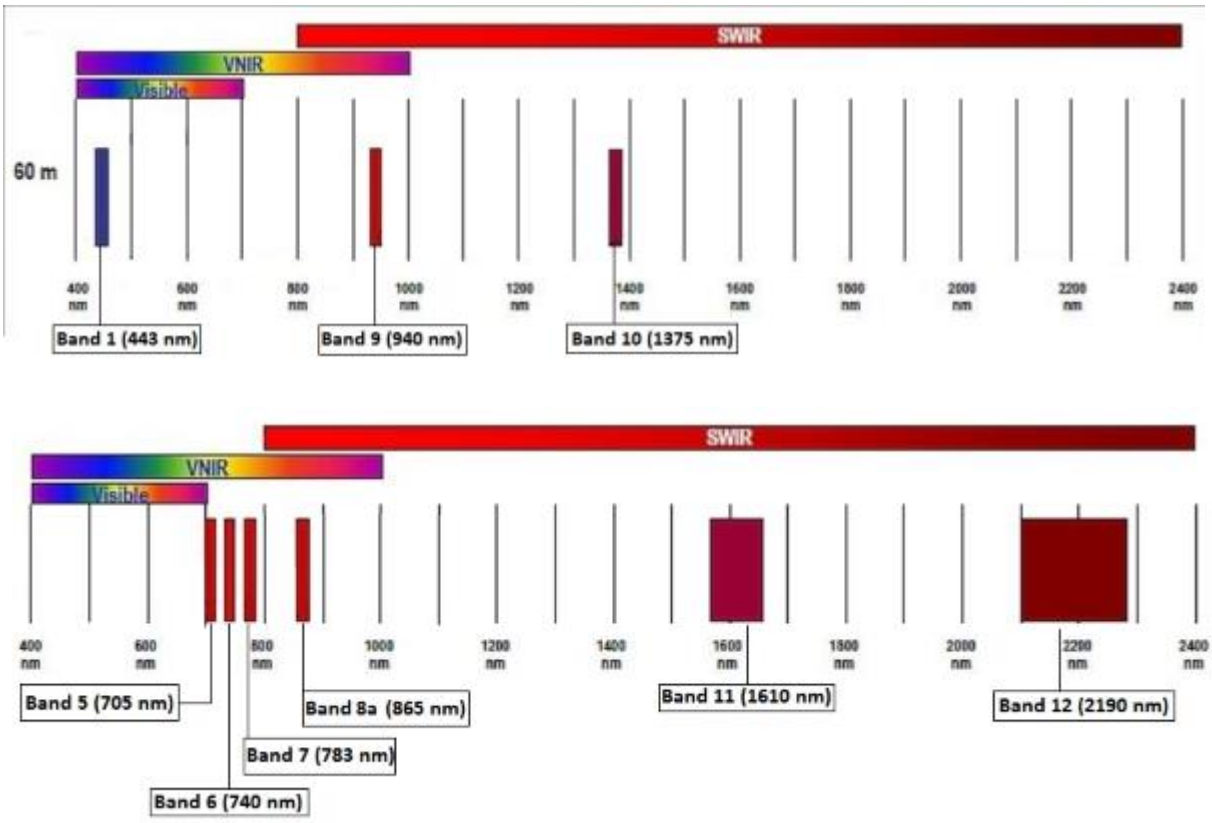

Figure 11 - Sentinel-2 spectral bands (ESA, User guides – Sentinel Online)

The Sentinel-2 satellites are equipped with a single multispectral instrument detecting 13 spectral intervals in the Visible (VIS), Near InfraRed (NIR), and Short-Wave InfraRed (SWIR). It is a push-broom imager with a 290 km large swath. The aperture is 150 mm and the focal length 600 mm, determining a FOV of 21° by 3,5°. Radiometric resolution is 12 bit, therefore brightness intensity ranges from 0 to 4095. As previously mentioned revisiting time is 5 days (10 days with a double satellite infrastructure).

The products are defined and distributed according to a different level of preprocessing. The main outputs are the following. Level 1-C products are *Top-of-atmosphere reflectance* in cartographic geometry (UTM projection on WGS84 ellipsoid). Level 2-A products are characterized by a correction providing *Surface reflectance* in cartographic geometry. This is the kind of output that can be used without further processing, and the one used in this work.

In this work we are going to use RGB imagery where spectral bands are respectively band 2= Blue (492,4 nm), band 3= Green (559,8 nm), band 4= Red (664,6 nm), each with a 10 m spatial resolution. In some case we are going to define a land mask using band 8= NIR (832,8 nm), again with 10 m spatial resolution.

UAV

In the case of Capo San Donato marina, the aerial imagery was acquired using an UAV. The drone is a Mini from DJI, utilized by Maifredi Geological Associated Studio. The output snapshot covers an area of 200x300 m^2 , seen from 30 m AGL (Above Ground Level). The spatial ground resolution is 1,3 cm.

Workflow

The operational workflow from data acquisition to the achievement of results, is peppered with assorted actions through platforms, software, and computations. This section is about that workflow, describing it in detail. The way is paved at first with the imagery download or snapshots acquisition, then the preprocessing phase follows, and later, during data extraction, foundations are laid for computations involving calibration and validation of the selected algorithm. At the end of the road a comparison between observed quantities and computed ones is performed.

Dataset preparation

The mentioned surveys provided the dataset. This is made up by acquired at different moments imagery. The Roja river aerial snapshots were taken in August 2019 and the SBES survey was performed on the 5th November 2019. For the Finale Ligure study, the SBES survey was conducted simultaneously with the drone flight, in January 2020.

In the case of the Roja river we downloaded imagery from the online open platform of Regione Liguria, the so-called regional geoportal (geoportal.regione.liguria.it). To download AGEA orthophotos, special credentials are required. This set of images had been already orthorectified and georeferenced, therefore ready to be used. For the marina in Finale Ligure, UAV imagery was used but equally orthorectified by the provider.

As empirical methods are based on the use of in-situ surveys, it is important to search for source images in a time window that is close to the bathymetric survey one.

To download satellite imagery, we resorted to the online platform Copernicus Open Access Hub (scihub.copernicus.eu). Here images can be sorted by sensing date or by the type of wanted product.

Figure 12 - Copernicus Open Access Hub opening page – ESA

The satellite snapshot had so to be coeval with the in-situ measurements and the aerial images to be compared with. Hence, we dealt with a large discrepancy between the datasets, but this was favorable allowing us to retrieve a satellite imagery within a large time-span. Another aspect to take into account is cloud cover. Any satellite photo with clouds covering the area to be addressed, results completely useless. This created some problem in finding the proper snapshot within the Ligurian fall. Another critical issue to consider when searching for the proper satellite images, is turbidity. As we stated in the previous sections turbidity can largely affect the results, if not even frustrate the whole effort.

The outcome of many evaluations was represented by the images taken on the 27th October and the 6th November 2019, for the Roja river. As we are going to see, a third choice was needed: the 14th October 2019. The Sentinel-2 image we picked for the Finale Ligure site, was relevant to the 11th February 2020 (Table 3).

		Surveys timing
ROJA	SBES	5th November 2019
	AGEA	13th August 2019
	S2	14th October 2019
FINALE	SBES	8th January 2020
	UAV	8th January 2020
	S2	11th February 2020

Table 3 - Data acquisition timing

S-2 images preprocessing using SNAP

The Sentinel-2 imagery previously downloaded consists of a compressed archive or *product* (.zip). This can be preprocessed using the software from ESA: SNAP. This piece of software allows us to unpack directly the archive containing image and metadata, with a simple drag and drop action. The input bands depict a 100x100km wide area, referenced to the WGS84 global ellipsoid and UTM projection. The spectral bands included in the product are more than 10, but for our purposes the RGB bands and the NIR band are enough. The preprocessing phase is becoming clear, as we get that we have to subset the area and the bands of interest from the original product, reproject the output subset and write it into a new file, to be later used. Another relevant part is resampling. We have to be sure all the bands we are going to use, have the same spatial resolution. That is why we add to the process a resampling stage, in which all the bands are resampled referring to Band 2 spatial m resolution. We remind that bands 2, 3, 4 and 8 are respectively Blue, Green, Red and Near-Infra-Red for Sentinel-2 platform. The SNAP-ESA program has a

convenient function allowing us to execute a batch processing, designing it with blocks of code. This one-time procedure is composed therefore by resampling, subsetting, reprojecting and writing. The outcome of this workflow is a .tif multi band image that can be easily loaded and displayed in QGIS, setting the scene for the next steps.

RGB preliminary analysis

At this point we have obtained all the data allowing us to start. The SBES data are imported into QGIS to create a shapefile (.shp and other related outputs) made up by points. Manipulating the attribute table of the vector object we can identify outliers or NaN values. The imagery of interest is imported into QGIS as raster format. The data can be crossed sampling with a layer from the other getting a final .csv, using specific QGIS functions. The first step consists in associating the spectral band values and the observed depth. With a graphical output we are able to appreciate if there is a correlation between the involved quantities, and if that image can be a robust dataset for our purpose. This kind of evaluation is quickly performed using a MATLAB script, that relates depth and each band. The potential slope that is to be seen in the diagrams, gives us information about their relation.

Figures 13 and 14 display the aforementioned outputs for each reference environment.

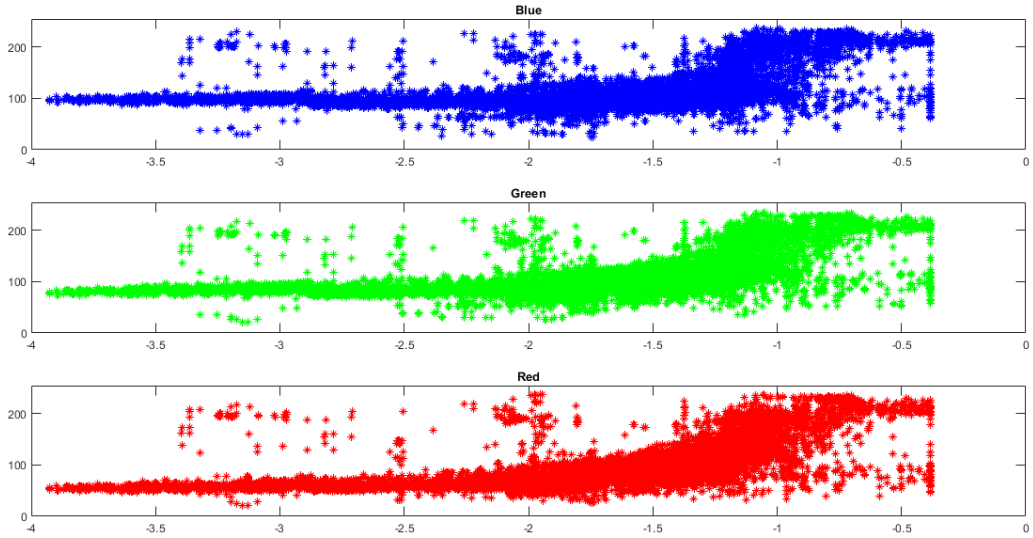

Figure 13 - Roja river AGEA RGB analysis

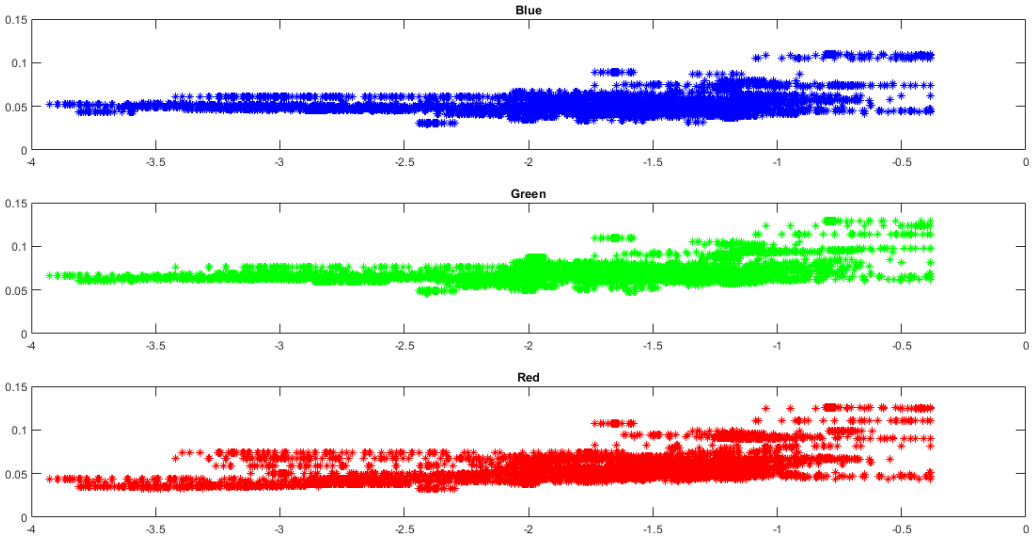

Figure 14 - Roja river Sentinel-2 RGB analysis on 27/10 image

Examining the two figures shows a relationship between depths and spectral band values.. However, it is somewhat concealed by the present amount of data, to be seen in the thickness of the colored lines. This takes us to the resampling phase.

Resampling

Roja River

For the Roja river we have the AGEA orthophoto with 20 cm resolution and the Sentinel-2 image with 10 m resolution. Both are related to the SBES points, which are 42585 points in the original vector file. We get that all those points, if combined with high horizontal resolution, can generate noise. Noise is any unwanted information coming from various sources such as sensors and instruments, space, interface, atmosphere etc. (Satellite Image Analysis: Clustering and Classification - Borra S Thanki R Dey N – 2019). Noise in satellite images affects the study or analysis, and this can show itself in confused diagrams. In our case we are getting too much information from the several surveys, resulting in data themselves masking the potential correlation.

Dealing with high spatial resolution is not always easy. In each pixel of the AGEA snapshot we have three SBES points. Three measurements in a 20 cm space. This is a huge amount of data considering the dimensions of our work, as we are dealing with a limited area with 0 to 4 m of depth range. Hence, we decided to resample both the orthophoto and the in-situ dataset. The orthophoto was resampled at 30 cm; and the SBES survey too, obtaining 11264 points. The RGB analysis improves its legibility (see Figure 15).

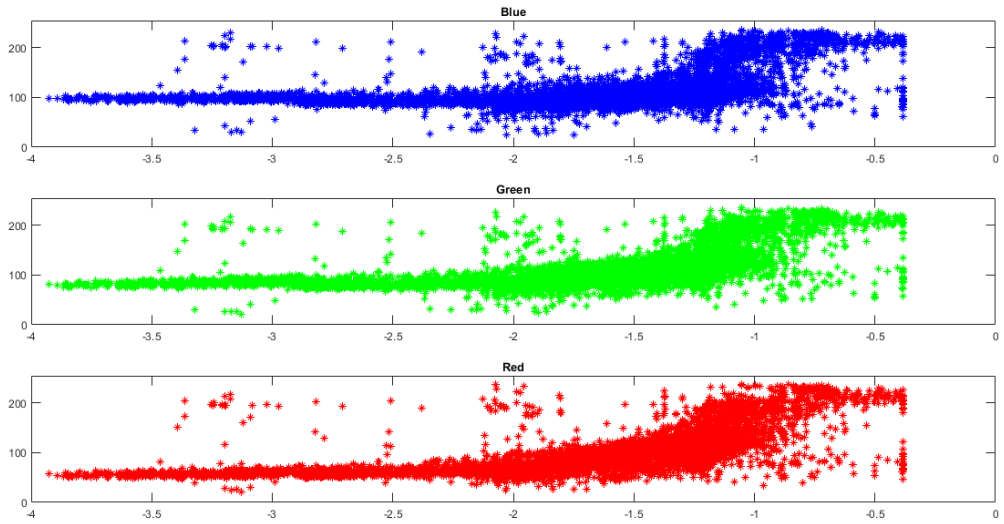

Figure 15 - Roja river AGEA RGB analysis after resampling at 30 cm

In this regard, we used a GRASS tool integrated into QGIS. Its name is *r.resample.stats.* This function gives the possibility to choose the statistical approach to be resorted to. We used the median method, rather than the mean, on account of the fact it is less affected by the noise magnitude.

As we wanted to remove further noise we tried to resample again both the orthophoto and the in-situ dataset at 1 m resolution, obtaining 3762 measurement points represented in the following scatter plots (Figure 16):

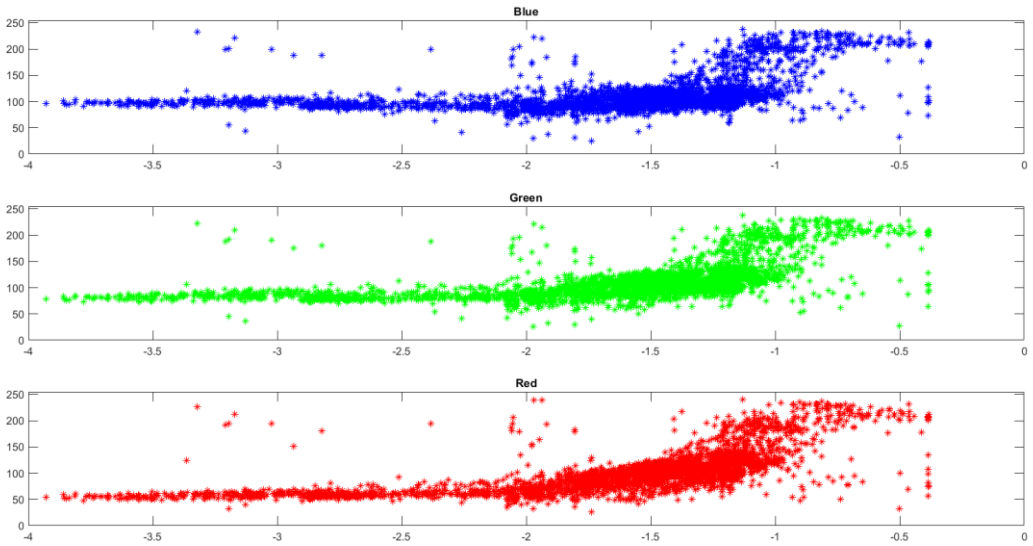

Figure 16 - Roja river AGEA RGB analysis after resampling at 1 m

As we can see there is some residual noise but the slope is highlighted, especially for the red band which presents a wider variation in the same depth range, this lets us hope for good results in later computations.

The related to Sentinel-2 SBES dataset was resampled too, picking 1500 random points. The diagram in Figure 17 is the outcome of its relation with the satellite image.

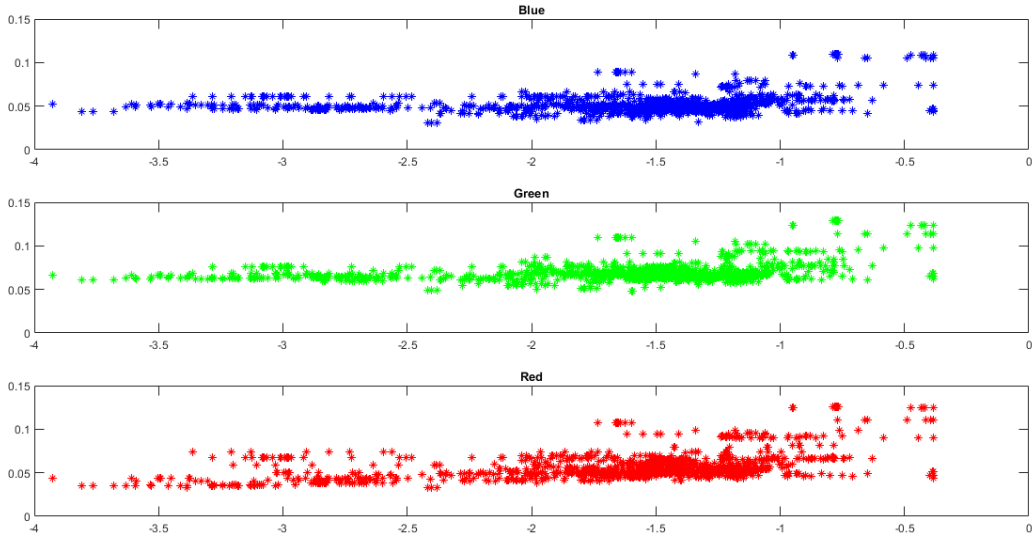

Figure 17 - Roja river Sentinel-2 RGB analysis on 27/10 image with 1500 random SBES points

Since the noise is visible and there is still a diversity in resolution between the raster image and the SBES vector points, we decided to equalize them getting a final dataset made up by a 10x10 m pixel satellite image and a set of measurements given by a point for each Sentinel-2 pixel, so 56 points.

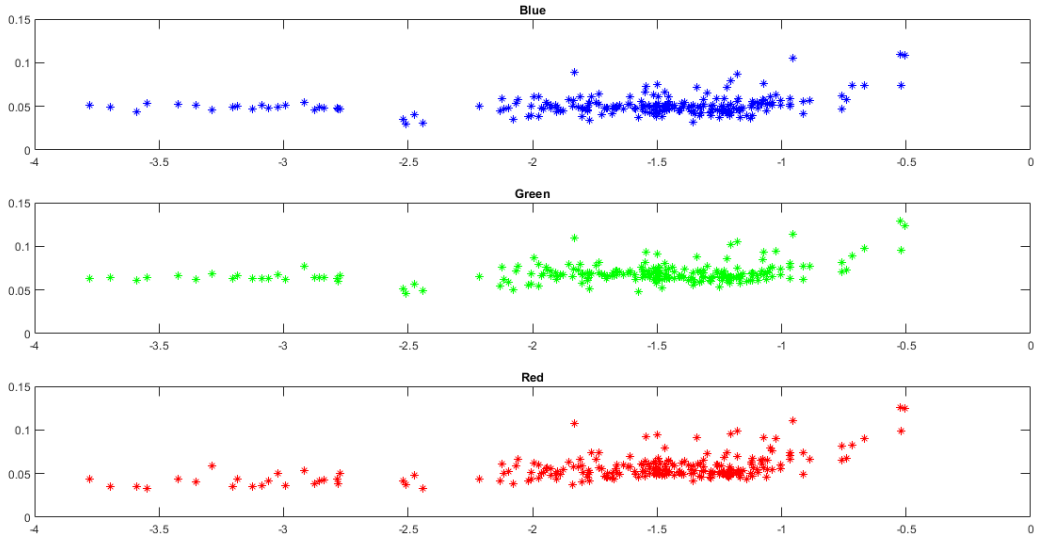

Figure 18 - Roja river Sentinel-2 RGB analysis on 27/10 image with 1 SBES point for each satellite pixel

Though the noise decreases the correlation is still hard to be highlighted for this case.

Since the results given by the Sentinel-2 imagery were not satisfying, another image was chosen. To properly select another picture, the hydrometric level time series were consulted. The Roja river witnessed, in fact, a higher water level phase after the 15th October 2019. We could reasonably assume this had been due to weather conditions variation, such as rainfalls, causing run-off and so increasing turbidity. Before these events the water level in the river showed no significant variations. The Figure 19 shows this change over time.

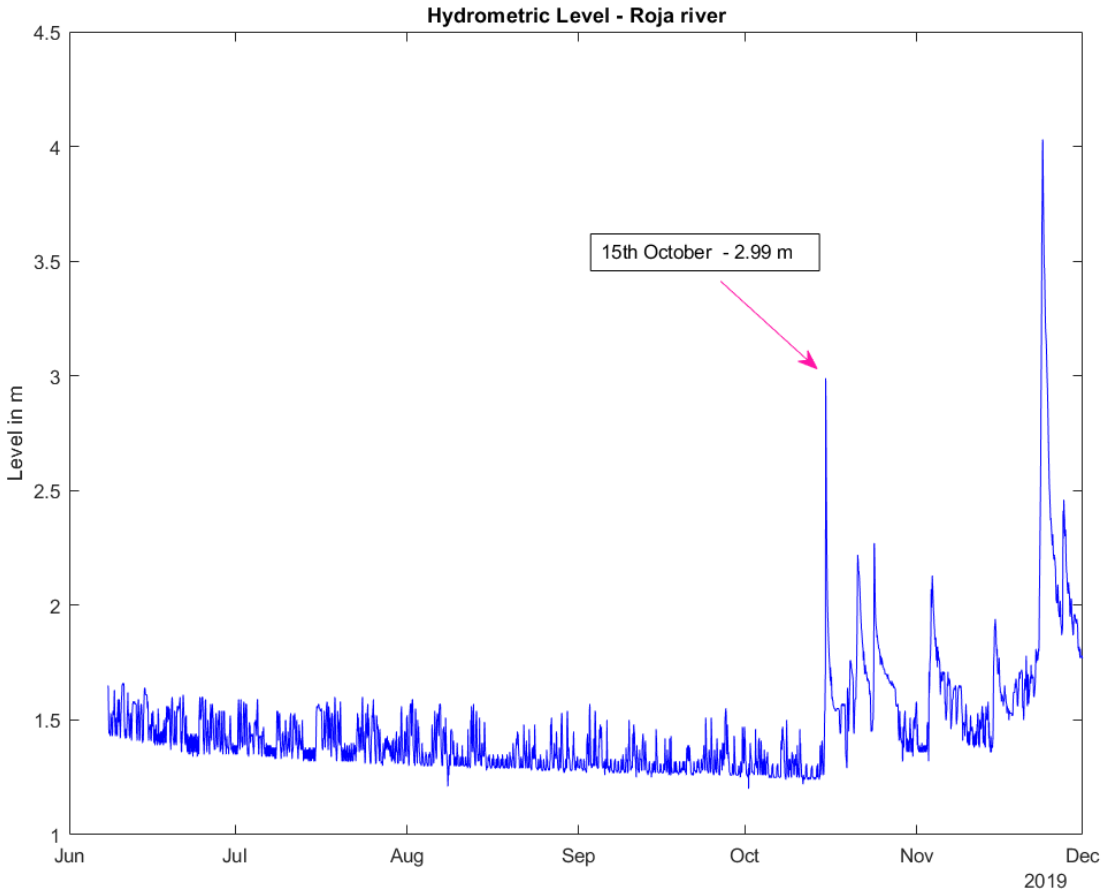

Figure 19 - Hydrometric Level in the Roja River in 2019 from SIRAL - Regione Liguria ©2005

The elected imagery refers so to the 14th October 2019. Being before the water level increasing event, this satellite snapshot looks promising in its RGB over depth diagram (Figure 20).

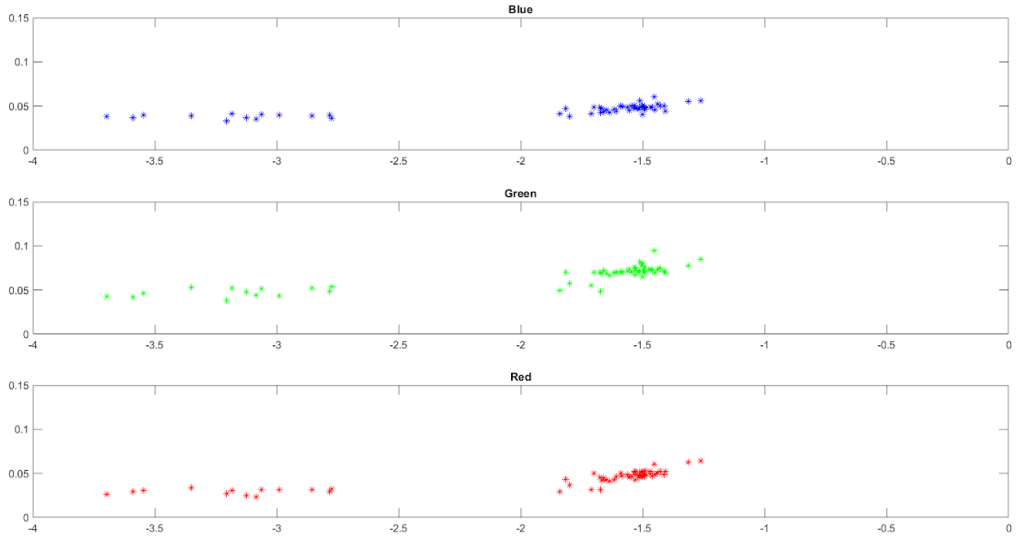

Figure 20 - - Roja river Sentinel-2 RGB analysis on 14/10 image with one SBES point for each satellite pixel

Finale Ligure

The same approach was applied to the Finale Ligure imagery, to assess its compliance with the consecutive stages. The results seemed good, with a promising correlation to be quantitively explored. The UAV orthophoto was anyhow resampled to 10 cm resolution. The following scatter plots (Figure 21 and 22) are referred to the UAV survey and Sentinel-2 imagery over the SBES depths measured at Capo San Donato marina.

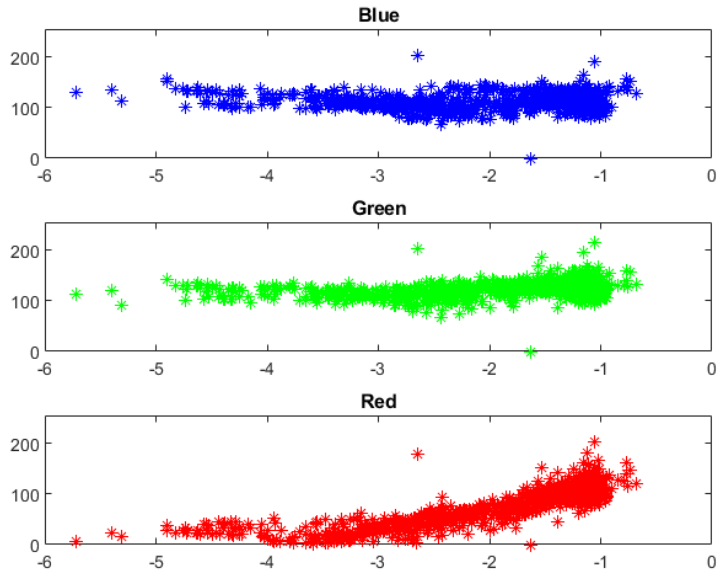

Figure 21 – Finale Ligure UAV RGB analysis

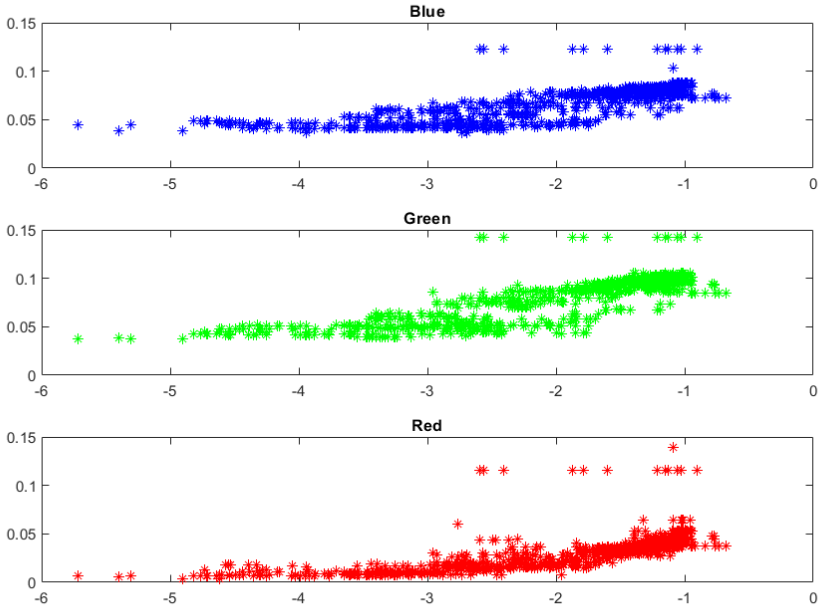

Figure 22 - Finale Ligure Sentinel-2 RGB analysis

Again we resampled the SBES points to have them to be uniform along the raster satellite image and its 10 m resolution.

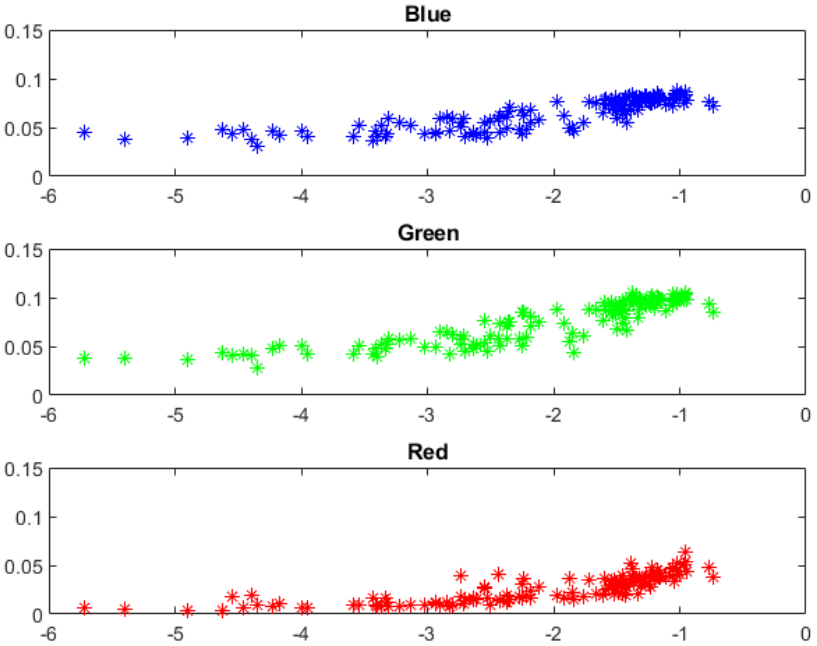

Figure 23 - Finale Ligure Sentinel-2 RGB analysis with 1 SBES point for each satellite pixel

Looking at the plots, the different spectral band response according to the water column absorption rate is to be appreciated (Kara et al., 2005).

At this point calibration and validation are to be performed, and we are going to address those in the coming sections.

Land mask detection using NIR spectral band

To increase the performance of the upcoming computations, a land mask is to be resorted to. In the case of aerial orthophotos we have to draw it manually, since no Near-InfraRed band is provided. The NIR spectral band can be used to mask land from the image, since the water appears dark and facilitates to discriminate water from land, which looks much brighter. The mask can be created with the use of a threshold value of the NIR band that separates land from sea.

This can be done in SNAP-ESA for satellite imagery. Accessing the *Band maths* section, we are able to convert the picture into a 0-1 values image. Where there is water the value is going to be 1, on the contrary 0 for land. This is achieved through an expression editor where we can state: *if B8 > 0.05 then NaN else 1.* B8 is, in our case, the number assigned to the NIR band (Serco Italia SPA, 2021). The threshold can be rearranged to get a better fitting of the land mask to the current situation.

For Roja river Sentinel-2 imagery a comparison between different thresholds was done. The Figure 24 gives an idea of the differences we can find. The showed colors are not referred to any spectral band, as we are dealing with the NIR band only.

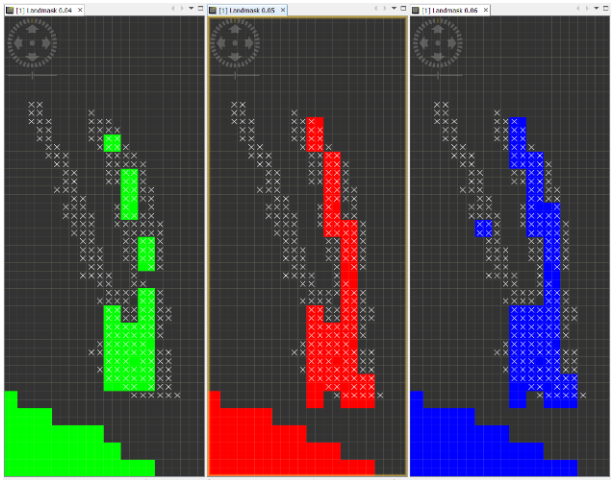

Figure 24 - NIR land mask thresholds for the Roja river dataset

We can see the 0,06 threshold (the blue one) is the one catching the highest number of water pixels within the SBES points represented with grey Xs. We picked it up as best-fitting value to build the land mask. After the land mask is completed, we can use it to extract just seen as water pixels from the original imagery.

The final outputs that follow are designed resorting to a common manual land mask, in order not to lose too much information.

Statistical parameters

Before entering into the core of the process, it is convenient to comment upon the several statistical parameters we are going to use. They allow to evaluate the results of our algorithm, informing us about the effectiveness of our work.

R^2

The coefficient of determination is a number describing a linear regression model, and if it can be used to make predictions. As a matter of fact, it tells us how much independent variables are effective in determining the dependent variables values. If values are too

scattered around the linear regression line, the model is less effective, on the contrary, when the values are fitting, it can be used to properly describe the studied phenomenon. Its formula:

$$R^2 = 1 - \frac{\sum_{i=1}^{n}(D_{SDBi} - D_{BFi})^2}{\sum_{i=1}^{n}\left(D_{BFi} - \overline{D_{BF}}\right)^2}$$

(3. 1)

Where D_{SDB} is the depth derived by satellite data, n is the number of the validation points, D_{BF} is the observed depth and $\overline{D_{BF}}$ is its mean value.

RMSE

Another parameter to take into account is the Root-Mean-Square Error ($RMSE$). This is an index assessing accuracy like R^2, but generally more dependent on the number of outliers. However, it is a convenient evaluation of the differences between observed values and computed ones. It is a non-negative descriptor and a value of 0 means impeccable fitting to the data. In our case if the value is, to make an example, 0,30 it means our model generally fails within 30 cm. $RMSE$ can be described as the square root of the average of squared errors. Its formula is the following, using previously seen notation:

$$RMSE = \sqrt{\frac{1}{n}\sum_{i=1}^{n}(D_{SDBi} - D_{BFi})^2}$$

(3. 2)

Additional parameters

At the end of the work, the results are going to be reported making use of additional parameters like Mean Absolute Error (MAE), whose formula is indicated below, or Bias Average (BIAS_AV).

$$MAE = \frac{1}{n}\sum_{i=1}^{n}|D_{SDBi} - D_{BFi}|$$

(3. 3)

In any case, it is given particular attention to the above presented R^2 and $RMSE$, since they provide us with an idea of the model effectiveness at a glance.

Band Ratio application

The empirical algorithm is now brought into play. In the first place, we have to use the Stumpf equation to compute the ratio for each band. As mentioned in the previous sections, we apply the logarithmic transformed in this triple appearance: Blue/Red, Blue/Green, Blue/Red + Blue/Green. This is done to try to improve results (Wei et al., 2021). With the QGIS *Raster calculator* we are able to determine the ratio between the raster images referring to the band of interest. The output we get is one raster layer for each ratio configuration, so three.

We have the designated set of points to be used as in-situ measurements, during next phase. The declared set is to be divided into two subsets, one of which accounting for 40% and the other for the remaining 60%. The former is used as calibration dataset, to determine the values of the tunable constants involved in the band ratio equation. The latter serves as validation dataset, to perform the final effective bathymetry derivation.

The calibration and validation datasets are vector layers made up by points. Sampling the raster values in QGIS the ratio value is associated to each point. This information is merged into a .csv file. This is a file containing essentially a table organizing the extracted values.

Output determination and computation

Using MATLAB we can manage and analyze tables and arrays as the variables of interest. The .csv is imported, and utilizing a script we can obtain the calibration results. Beside the statistical parameters, $m_1$and m_0 are derived, and they turn out to be fundamental in the next steps. In fact, calibration is represented by the moment in which we measure the relation between ratio and in situ depths to build a tuned bathymetry model to be applied on the whole water surfaces of the image. The results are finally evaluated with the validation dataset.

We see that there is a part of the initial set of measurements that is used to calibrate the algorithm, which is to be used later with the other part of data. The choice of the points subdivision is entrusted to the software, as it selects them randomly. In our case the calibration-validation stage was performed more than once, using a different random subdivision each time. The iterations of this part of the workflow were so distributed: 3 repetitions with a 40:60 proportion and 1 repetition with a 50:50 division. This was intended to be performed for each band ratio of each employed platform (satellite, UAV etc.). Where a high introduced variability had been acknowledged, another set of as mentioned reiterations was performed. For instance this is the case of satellite imagery, for which a set made up by 6 cycles at 40:60 and 2 at 50:50 was performed .

The final passage of our roadmap is represented by the comparison between the observed depth and the computed one. This is a pivotal moment in the assessment of the utilized algorithm's effectiveness.

Results Presentation

The current section deals with the presentation of numerical and graphical results. These are based on the processing using QGIS and the operated with MATLAB computations. Specifically, the showed diagrams are the direct output from MATLAB execution. We are

going to address the results of calibration process compared with the validation ones. This is going to be repeated for each kind of imagery recursively. The calibration outcome is always depicted in blue, conversely validation is illustrated using the color it is referred to, so: red, green, and magenta for the bands sum. Since more than one iteration for each band and platform has been carried out, the showed diagrams are referred to the best-performing cycle, for sake of space. The complete set of iterations is only presented in the final data tables.

Roja River

Let us begin with the outcome relative to the Roja river. Here two mentioned platforms have been used: aerial orthophoto and Sentinel-2 imagery. The analysis of results is starting with the orthophoto and proceeding with the other.

AGEA Imagery

The orthophoto analysis has been performed 4 times and here related diagrams are to be seen (Figure 25, 26, 27). They are paired into calibration-validation sets, as previously stated.

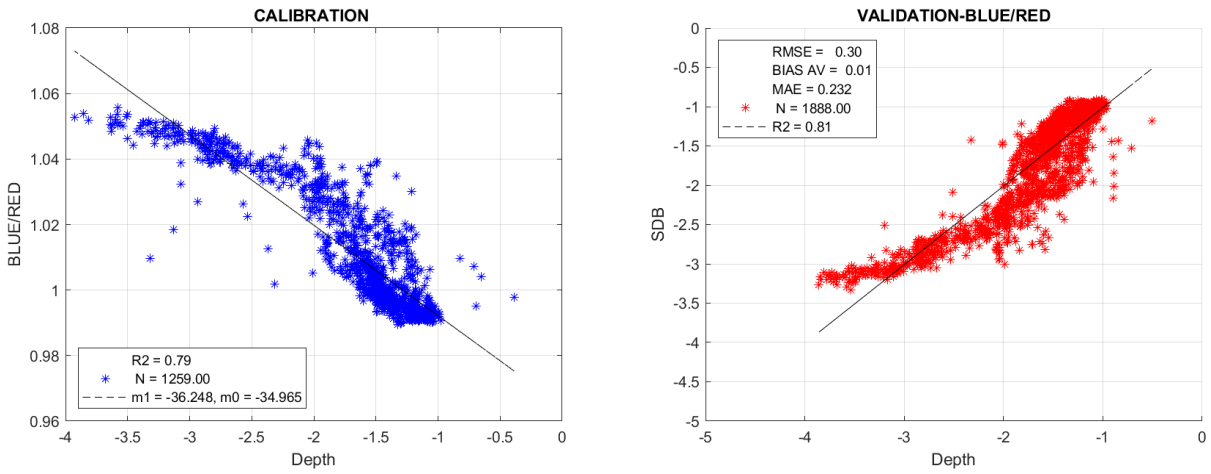

Figure 25 - Aerial Orthophoto of Roja river - Set of calibration and validation for the red band

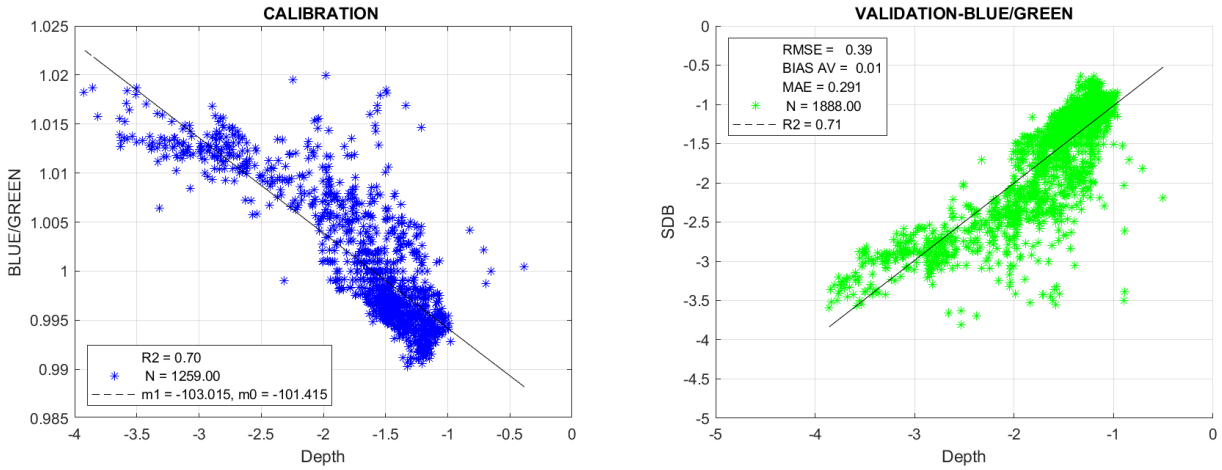

Figure 26 - Aerial Orthophoto of Roja river - Set of calibration and validation for the green band

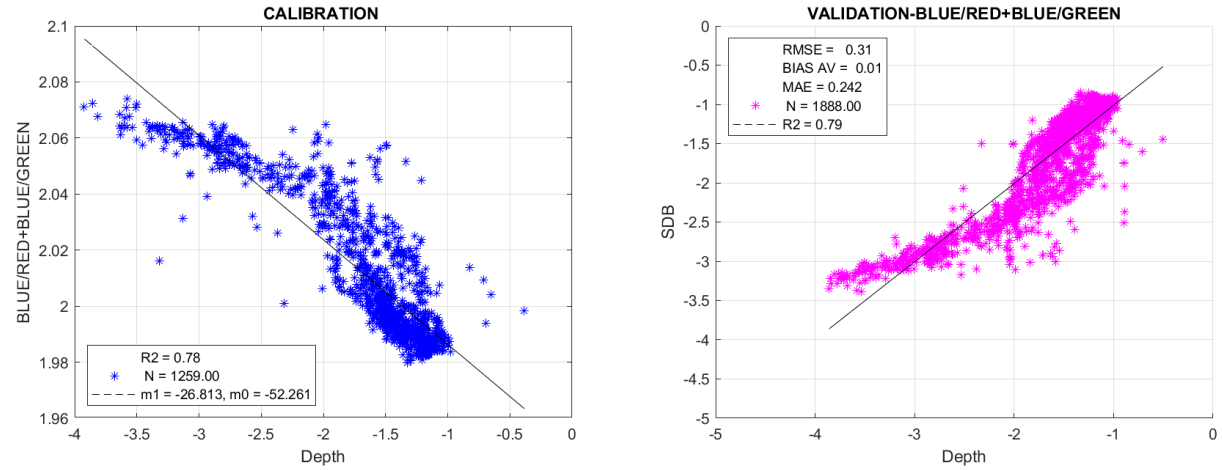

Figure 27 - Aerial Orthophoto of Roja river - Set of calibration and validation for the sum of bands

The Figure 28 represents the bias distribution of the best-performing band among the above ones, referring to the total amount of points being 1888.

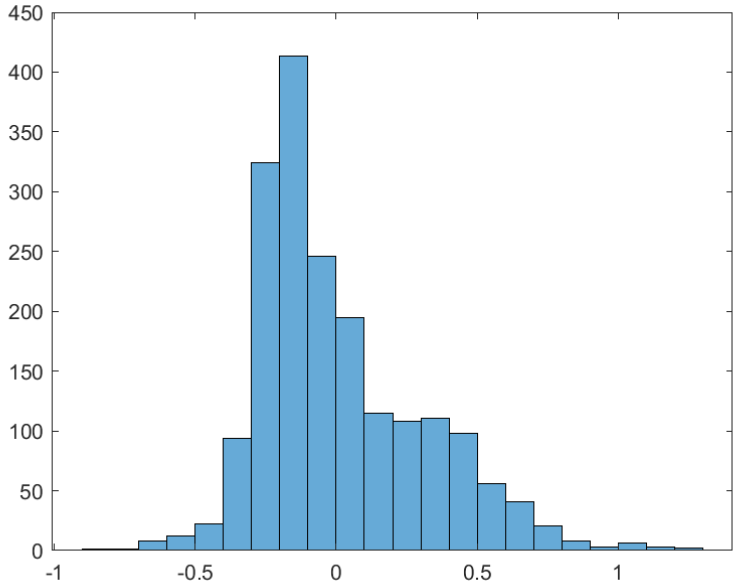

Figure 28 - Aerial Orthophoto of Roja river – Bias distribution for RED band

Sentinel-2 imagery

The Sentinel-2 snapshots analysis has been performed 8 times and here the best-performing iteration of satellite imagery processing is to be found (Figure 29, 30, 31).

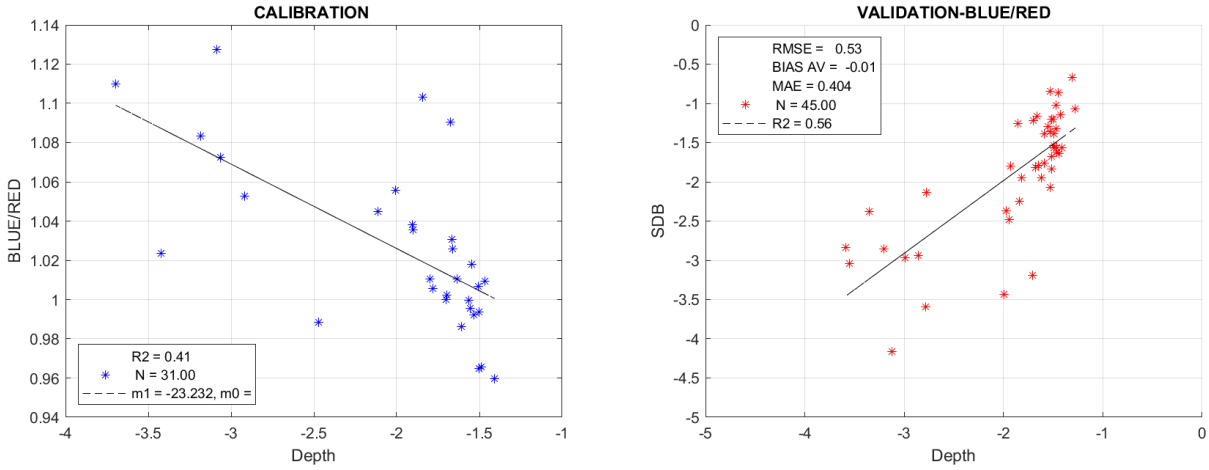

Figure 29 - Sentinel-2 imagery of Roja river - Set of calibration and validation for the red band

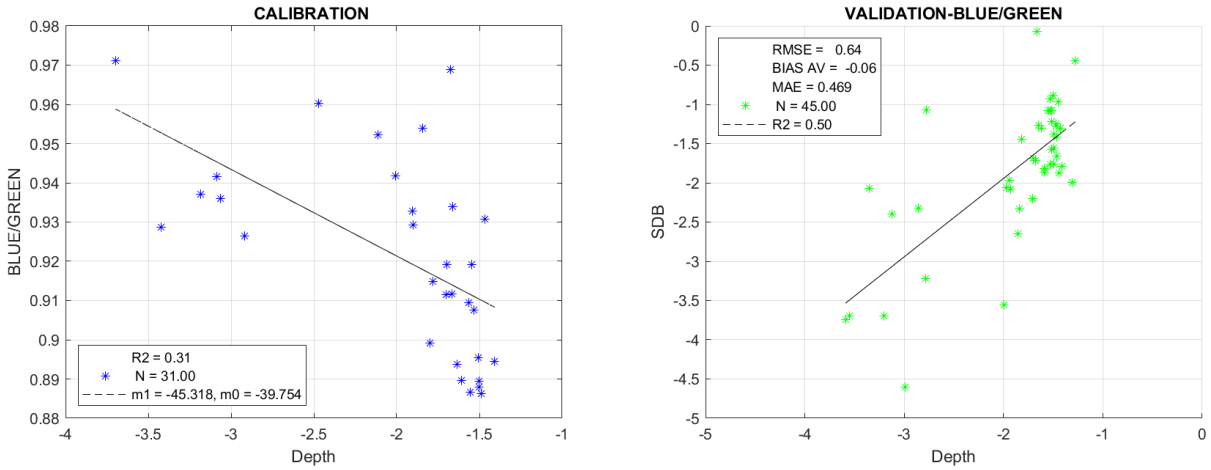

Figure 30 - Sentinel-2 imagery of Roja river - Set of calibration and validation for the green band

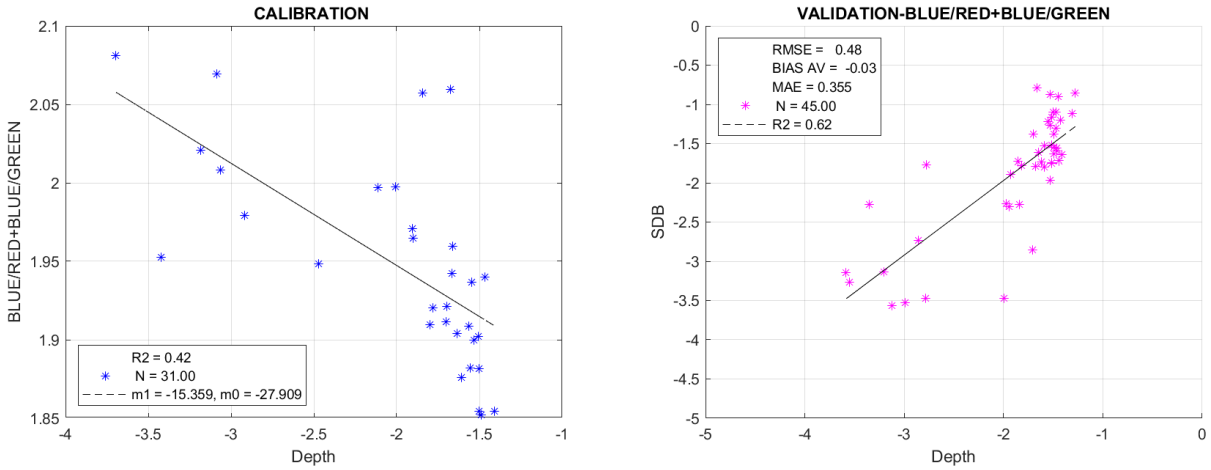

Figure 31 - Sentinel-2 imagery of Roja river - Set of calibration and validation for the sum of bands

The Figure 32 represents the bias distribution of the best-performing band among the above ones, referring to the total amount of points being 45.

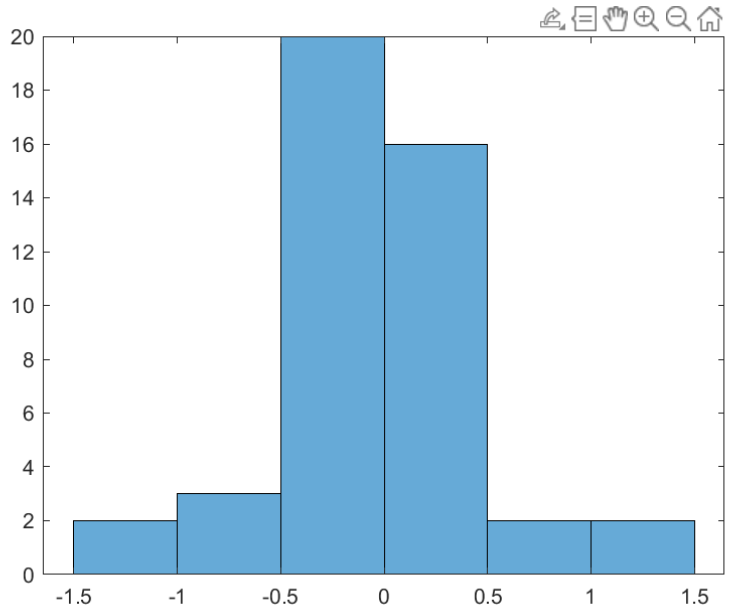

Figure 32 - Sentinel-2 imagery of Roja river - Bias distribution for the sum of bands (B/R + B/G)

Tables and graphical outputs

Calibration and validation values are reported in Tables 4 and 5. They encompass the whole set of iterations of each utilized platform, for this specific study site. Included are the previously described statistical parameters. Where the iteration is characterized by a 50:50 ratio between calibration and validation datasets, a 50% is depicted. Otherwise, the ratio is 40:60. In Figure 33, the graphical output from QGIS processing is to be seen. This is a raster representing derived bathymetry. The difference in spatial resolution can be appreciated.

AGEA

BLUE/RED			
CAL 1		VAL 1	
N°	1259	**N°**	1888
m1	-36.248	**RMSE**	0.295
m0	-34.965	**BIAS_AV**	0.011
R2	0.789	**MAE**	0.232
CAL 2		VAL 2	
N°	1259	**N°**	1888
m1	-36.760	**RMSE**	0.303
m0	-35.493	**BIAS_AV**	-0.004

BLUE/GREEN			
CAL 1		VAL 1	
N°	1259	**N°**	1888
m1	-103.015	**RMSE**	0.388
m0	-101.415	**BIAS_AV**	0.006
R2	0.702	**MAE**	0.291
CAL 2		VAL 2	
N°	1259	**N°**	1888
m1	-103.939	**RMSE**	0.393
m0	-102.351	**BIAS_AV**	-0.013

BLUE/RED + BLUE/GREEN			
CAL 1		VAL 1	
N°	1259	**N°**	1888
m1	-26.813	**RMSE**	0.310
m0	-52.261	**BIAS_AV**	0.010
R2	0.776	**MAE**	0.242
CAL 2		VAL 2	
N°	1259	**N°**	1888
m1	-27.156	**RMSE**	0.317
m0	-52.961	**BIAS_AV**	-0.007

R2	0.798	**MAE**	0.239
CAL 3		VAL 3	
N°	1259	**N°**	1888
m1	-36.585	**RMSE**	0.296
m0	-35.326	**BIAS_AV**	-0.020
R2	0.789	**MAE**	0.240
CAL 4 50%		VAL 4 50%	
N°	1573	**N°**	1574
m1	-36.404	**RMSE**	0.304
m0	-35.119	**BIAS_AV**	0.023
R2	0.814	**MAE**	0.236

R2	0.711	**MAE**	0.295
CAL 3		VAL 3	
N°	1259	**N°**	1888
m1	-105.763	**RMSE**	0.380
m0	-104.190	**BIAS_AV**	-0.034
R2	0.668	**MAE**	0.297
CAL 4 50%		VAL 4 50%	
N°	1573	**N°**	1574
m1	-104.621	**RMSE**	0.404
m0	-103.010	**BIAS_AV**	0.034
R2	0.724	**MAE**	0.300

R2	0.785	**MAE**	0.248
CAL 3		VAL 3	
N°	1259	**N°**	1888
m1	-27.182	**RMSE**	0.309
m0	-53.025	**BIAS_AV**	-0.024
R2	0.767	**MAE**	0.250
CAL 4 50%		VAL 4 50%	
N°	1573	**N°**	1574
m1	-27.007	**RMSE**	0.321
m0	-52.644	**BIAS_AV**	0.026
R2	0.800	**MAE**	0.247

Table 4 - Roja river orthophoto results

Sentinel-2

BLUE/RED			
CAL 1		VAL 1	
N°	31	**N°**	45
m1	-20.039	**RMSE**	0.620
m0	-18.481	**BIAS_AV**	0.139
R2	0.527	**MAE**	0.466
CAL 2		VAL 2	
N°	31	**N°**	45
m1	-19.694	**RMSE**	0.593
m0	-18.248	**BIAS_AV**	-0.060
R2	0.670	**MAE**	0.434
CAL 3		VAL 3	
N°	31	**N°**	45
m1	-24.355	**RMSE**	0.651
m0	-22.900	**BIAS_AV**	0.135
R2	0.501	**MAE**	0.480
CAL 4 50%		VAL 4 50%	
N°	38	**N°**	38
m1	-21.340	**RMSE**	0.627
m0	-20.016	**BIAS_AV**	-0.242
R2	0.467	**MAE**	0.480
CAL 5		VAL 5	
N°	31	**N°**	45
m1	-18.762	**RMSE**	0.595
m0	-17.173	**BIAS_AV**	0.141
R2	0.697	**MAE**	0.412
CAL 6		VAL 6	
N°	31	**N°**	45
m1	-26.469	**RMSE**	0.785
m0	-25.073	**BIAS_AV**	0.117
R2	0.502	**MAE**	0.570

BLUE/GREEN			
CAL 1		VAL 1	
N°	31	**N°**	45
m1	-37.224	**RMSE**	0.673
m0	-32.144	**BIAS_AV**	0.230
R2	0.370	**MAE**	0.512
CAL 2		VAL 2	
N°	31	**N°**	45
m1	-43.408	**RMSE**	0.777
m0	-37.895	**BIAS_AV**	0.119
R2	0.500	**MAE**	0.569
CAL 3		VAL 3	
N°	31	**N°**	45
m1	-42.400	**RMSE**	0.647
m0	-36.939	**BIAS_AV**	0.167
R2	0.406	**MAE**	0.509
CAL 4 50%		VAL 4 50%	
N°	38	**N°**	38
m1	-48.633	**RMSE**	0.765
m0	-42.949	**BIAS_AV**	-0.242
R2	0.239	**MAE**	0.480
CAL 5		VAL 5	
N°	31	**N°**	45
m1	-35.361	**RMSE**	0.678
m0	-30.511	**BIAS_AV**	0.093
R2	0.624	**MAE**	0.529
CAL 6		VAL 6	
N°	31	**N°**	45
m1	-39.313	**RMSE**	0.677
m0	-34.062	**BIAS_AV**	0.235
R2	0.444	**MAE**	0.494

BLUE/RED + BLUE/GREEN			
CAL 1		VAL 1	
N°	31	**N°**	45
m1	-13.027	**RMSE**	0.562
m0	-23.266	**BIAS_AV**	0.171
R2	0.509	**MAE**	0.410
CAL 2		VAL 2	
N°	31	**N°**	45
m1	-13.574	**RMSE**	0.584
m0	-24.379	**BIAS_AV**	-0.007
R2	0.694	**MAE**	0.418
CAL 3		VAL 3	
N°	31	**N°**	45
m1	-15.469	**RMSE**	0.560
m0	-28.022	**BIAS_AV**	0.146
R2	0.512	**MAE**	0.403
CAL 4 50%		VAL 4 50%	
N°	38	**N°**	38
m1	-14.832	**RMSE**	0.586
m0	-27.010	**BIAS_AV**	-0.278
R2	0.432	**MAE**	0.478
CAL 5		VAL 5	
N°	31	**N°**	45
m1	-12.258	**RMSE**	0.585
m0	-21.797	**BIAS_AV**	0.124
R2	0.779	**MAE**	0.419
CAL 6		VAL 6	
N°	31	**N°**	45
m1	-15.818	**RMSE**	0.638
m0	-28.690	**BIAS_AV**	0.164
R2	0.520	**MAE**	0.437

CAL 7		VAL 7	
N°	31	N°	45
m1	-23.232	RMSE	0.526
m0	-21.836	BIAS_AV	-0.009
R2	0.408	MAE	0.404
CAL 8 50%		VAL 8 50%	
N°	38	N°	38
m1	-23.572	RMSE	0.615
m0	-22.211	BIAS_AV	-0.067
R2	0.510	MAE	0.473

CAL 7		VAL 7	
N°	31	N°	45
m1	-45.318	RMSE	0.642
m0	-39.754	BIAS_AV	-0.056
R2	0.314	MAE	0.469
CAL 8 50%		VAL 8 50%	
N°	38	N°	38
m1	-44.825	RMSE	0.855
m0	-39.249	BIAS_AV	0.039
R2	0.526	MAE	0.631

CAL 7		VAL 7	
N°	31	N°	45
m1	-15.359	RMSE	0.480
m0	-27.909	BIAS_AV	-0.025
R2	0.422	MAE	0.355
CAL 8 50%		VAL 8 50%	
N°	38	N°	38
m1	-15.448	RMSE	0.631
m0	-28.083	BIAS_AV	-0.030
R2	0.589	MAE	0.471

Table 5 - Roja river Sentinel-2 results

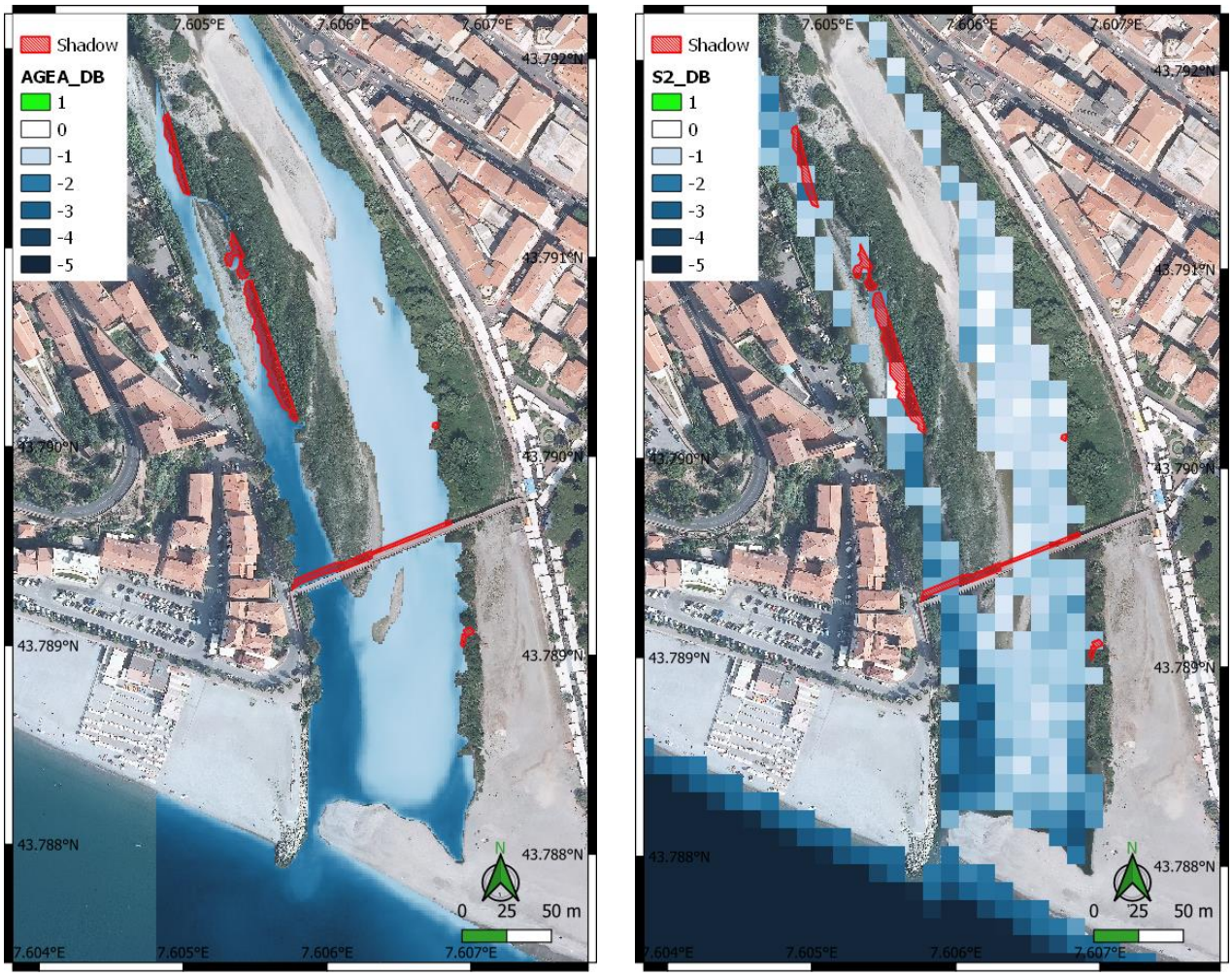

Figure 33 - Derived bathymetry for Roja river using AGEA orthophoto (left) and Sentinel-2 imagery (right), the same manual land mask is applied.

Finale Ligure

The same outcome representation is achieved for the Capo San Donato data. Results are equally showed for both used platforms, which are the drone orthophoto and the Sentinel-2 imagery.

UAV imagery

The drone orthophoto analysis has been performed 8 times and here related diagrams are to be seen (Figure 34, 35, 36). They are paired into calibration-validation sets, as previously seen.

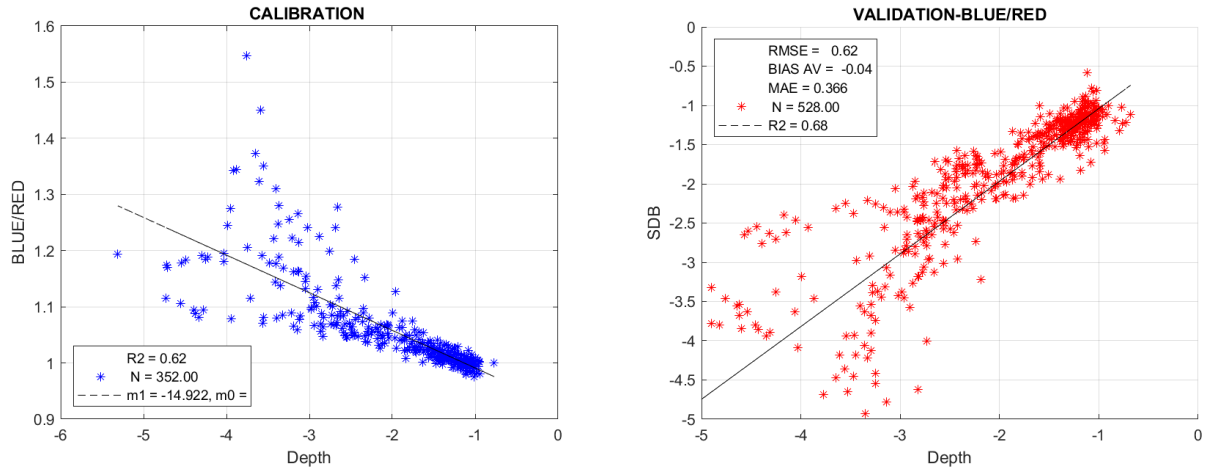

Figure 34 - UAV Orthophoto of Capo San Donato - Set of calibration and validation for the red band

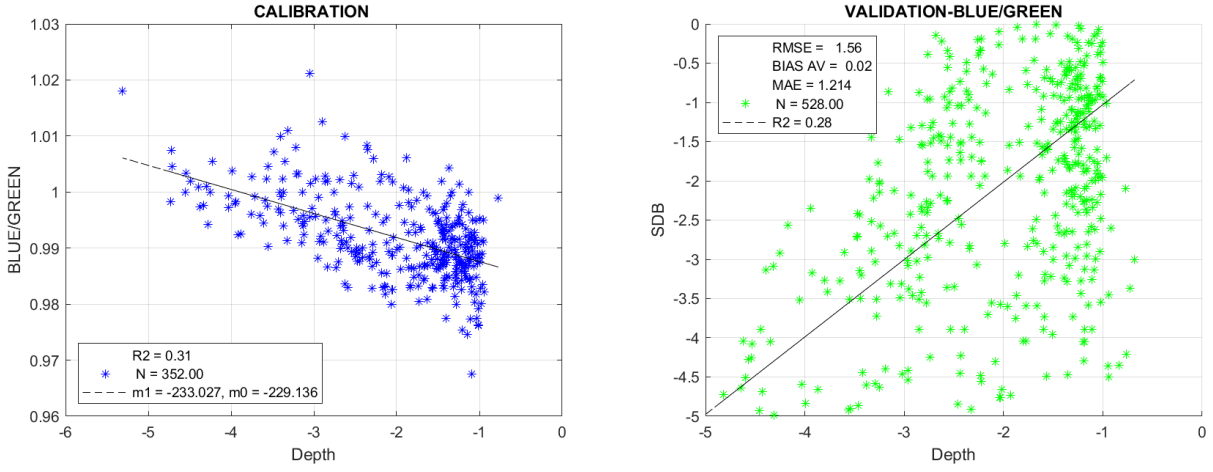

Figure 35 - UAV Orthophoto of Capo San Donato - Set of calibration and validation for the green band

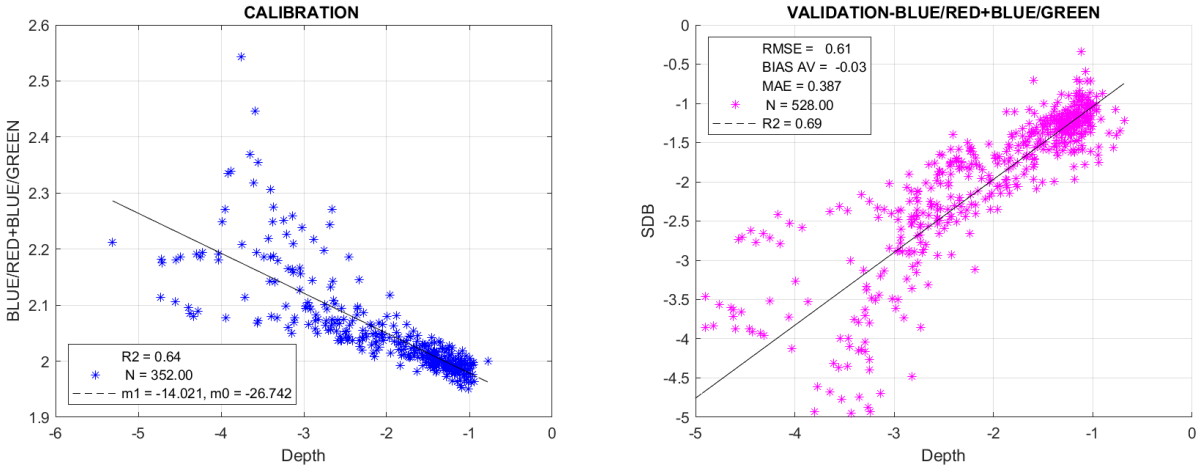

Figure 36 - UAV Orthophoto of Capo San Donato - Set of calibration and validation for the sum of bands

The Figure 37 represents the bias distribution of the best-performing band among the above ones, referring to the total amount of points being 528.

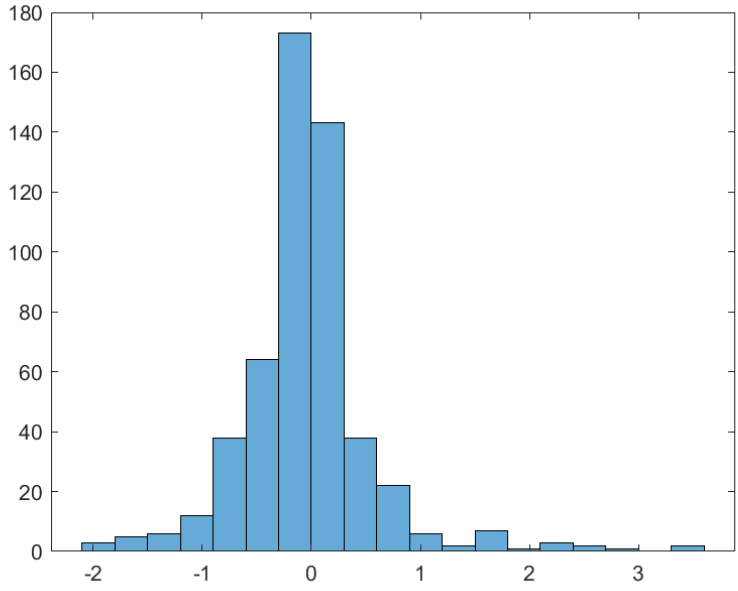

Figure 37 - UAV Orthophoto of Capo San Donato - Bias distribution for the sum of bands (B/R + B/G)

Sentinel-2 imagery

The Sentinel-2 snapshots analysis has been performed 8 times and here the best-performing iteration of satellite imagery processing is to be found (Figure 38, 39, 40).

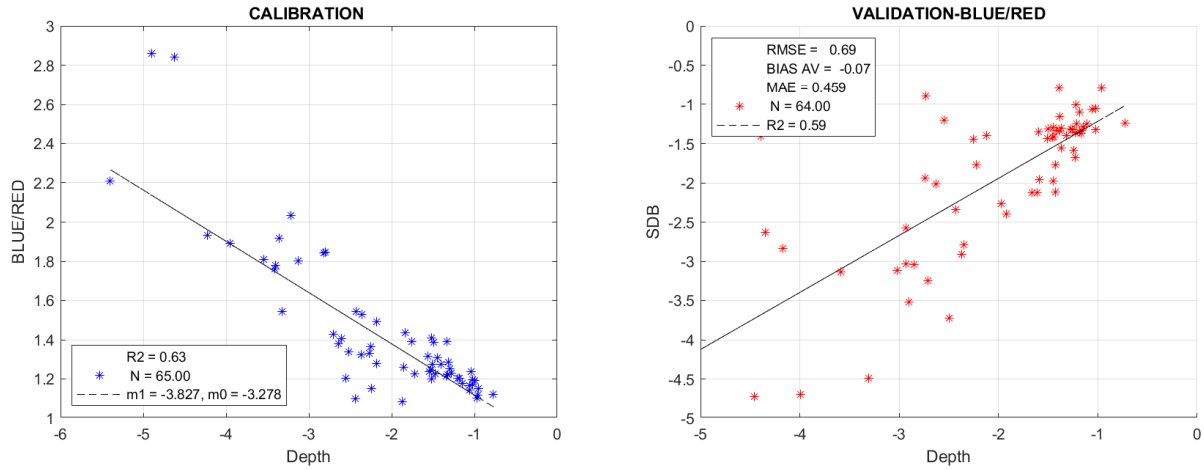

Figure 38 - Sentinel-2 imagery of Capo San Donato - Set of calibration and validation for the red band

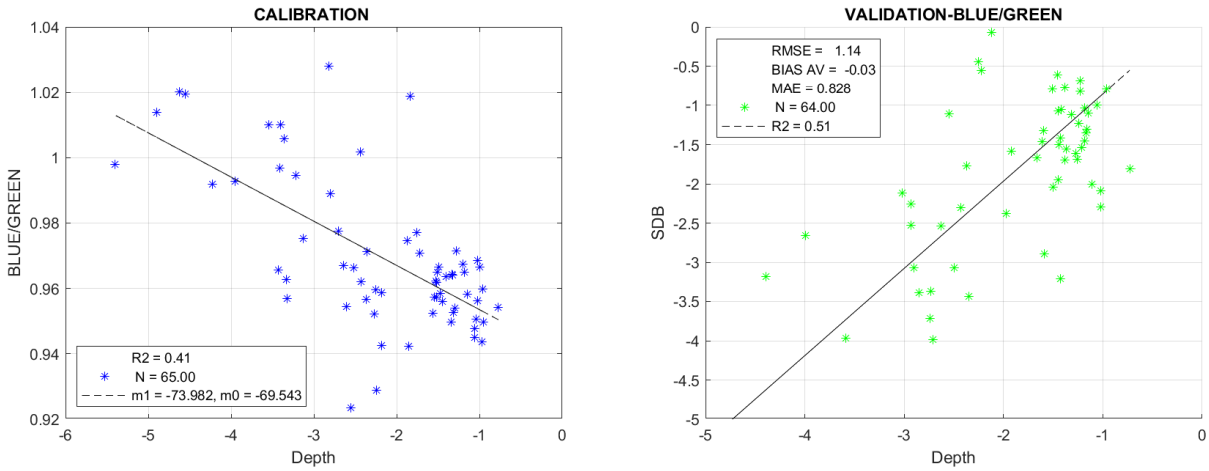

Figure 39 - Sentinel-2 imagery of Capo San Donato - Set of calibration and validation for the green band

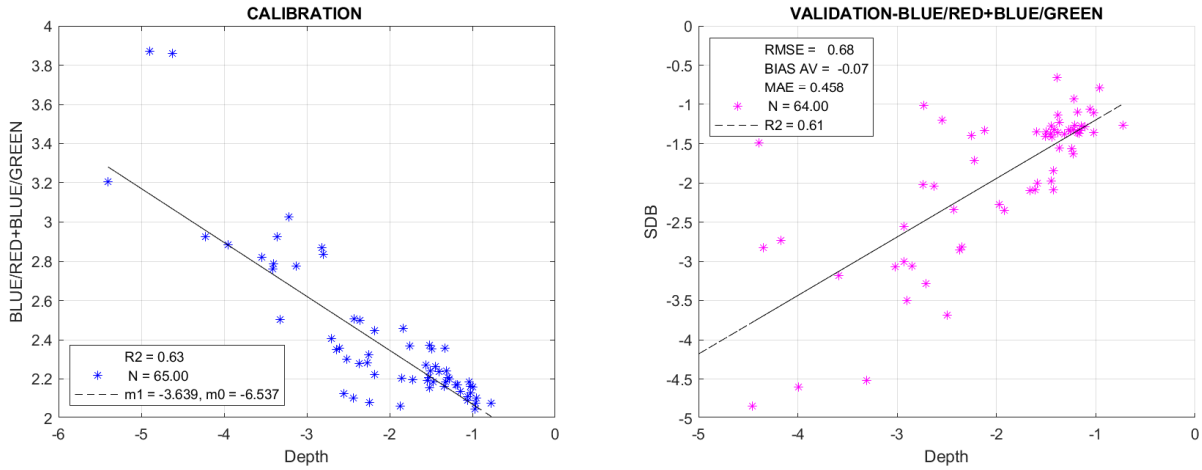

Figure 40 - Sentinel-2 imagery of Capo San Donato - Set of calibration and validation for the sum of bands

The Figure 41 represents the bias distribution of the best-performing band among the above ones, referring to the total amount of points being 64.

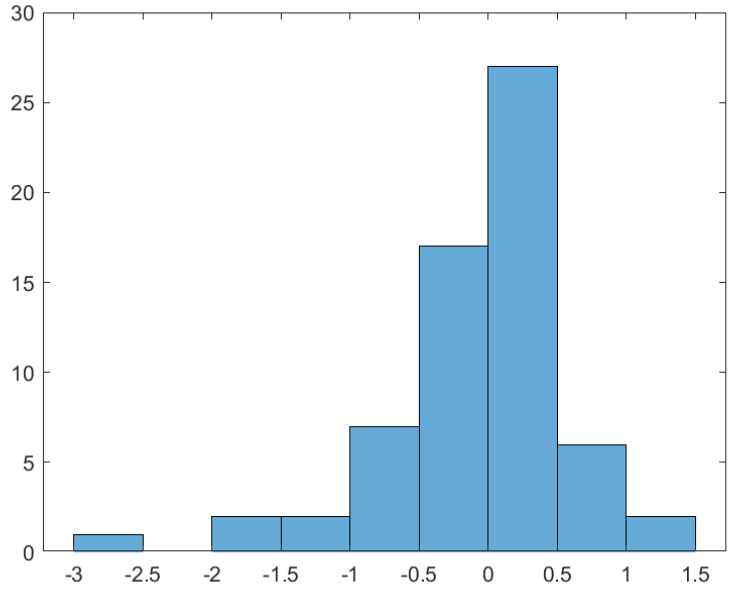

Figure 41 - Sentinel-2 imagery of Capo San Donato - Bias distribution for the sum of bands (B/R + B/G)

Tables and graphical outputs

Calibration and validation values are reported in Tables 6 and 7. They encompass the whole set of iterations of each utilized platform, for this specific study site. Included are the previously described statistical parameters. Where the iteration is characterized by a 50:50 ratio between calibration and validation datasets, a 50% is depicted. Otherwise, the ratio is 40:60. In Figure 42, the graphical output from QGIS processing is to be seen. This is a raster representing derived bathymetry. The difference in spatial resolution can be appreciated.

UAV

BLUE/RED			
CAL 1		VAL 1	
N°	352	**N°**	528
m1	-16.110	**RMSE**	0.709
m0	-15.004	**BIAS_AV**	0.031
R2	0.647	**MAE**	0.388
CAL 2		VAL 2	
N°	352	**N°**	528
m1	-15.454	**RMSE**	0.707
m0	-14.334	**BIAS_AV**	-0.009
R2	0.668	**MAE**	0.386
CAL 3		VAL 3	
N°	352	**N°**	528
m1	-16.245	**RMSE**	0.754
m0	-15.136	**BIAS_AV**	0.049
R2	0.673	**MAE**	0.399
CAL 4 50%		VAL 4 50%	
N°	440	**N°**	440
m1	-15.657	**RMSE**	0.719
m0	-14.551	**BIAS_AV**	-0.015
R2	0.667	**MAE**	0.391
CAL 5		VAL 5	
N°	352	**N°**	528
m1	-14.010	**RMSE**	0.649
m0	-12.841	**BIAS_AV**	-0.066
R2	0.671	**MAE**	0.388
CAL 6		VAL 6	
N°	352	**N°**	528
m1	-14.922	**RMSE**	0.624

BLUE/GREEN			
CAL 1		VAL 1	
N°	352	**N°**	528
m1	-234.486	**RMSE**	1.504
m0	-230.646	**BIAS_AV**	-0.090
R2	0.308	**MAE**	1.170
CAL 2		VAL 2	
N°	352	**N°**	528
m1	-230.118	**RMSE**	1.484
m0	-226.200	**BIAS_AV**	0.098
R2	0.296	**MAE**	1.157
CAL 3		VAL 3	
N°	352	**N°**	528
m1	-221.810	**RMSE**	1.434
m0	-218.060	**BIAS_AV**	-0.073
R2	0.331	**MAE**	1.137
CAL 4 50%		VAL 4 50%	
N°	440	**N°**	440
m1	-239.149	**RMSE**	1.533
m0	-235.198	**BIAS_AV**	0.041
R2	0.285	**MAE**	1.210
CAL 5		VAL 5	
N°	352	**N°**	528
m1	-257.542	**RMSE**	1.625
m0	-253.512	**BIAS_AV**	-0.081
R2	0.212	**MAE**	1.270
CAL 6		VAL 6	
N°	352	**N°**	528
m1	-233.027	**RMSE**	1.559

BLUE/RED + BLUE/GREEN			
CAL 1		VAL 1	
N°	352	**N°**	528
m1	-15.075	**RMSE**	0.686
m0	-28.870	**BIAS_AV**	0.024
R2	0.661	**MAE**	0.407
CAL 2		VAL 2	
N°	352	**N°**	528
m1	-14.483	**RMSE**	0.684
m0	-27.670	**BIAS_AV**	-0.002
R2	0.680	**MAE**	0.404
CAL 3		VAL 3	
N°	352	**N°**	528
m1	-15.136	**RMSE**	0.725
m0	-28.984	**BIAS_AV**	0.041
R2	0.687	**MAE**	0.421
CAL 4 50%		VAL 4 50%	
N°	440	**N°**	440
m1	-14.697	**RMSE**	0.698
m0	-28.113	**BIAS_AV**	-0.011
R2	0.680	**MAE**	0.412
CAL 5		VAL 5	
N°	352	**N°**	528
m1	-13.284	**RMSE**	0.635
m0	-25.251	**BIAS_AV**	-0.067
R2	0.678	**MAE**	0.402
CAL 6		VAL 6	
N°	352	**N°**	528
m1	-14.021	**RMSE**	0.614

m0	-13.788	**BIAS_AV**	-0.036
R2	0.621	**MAE**	0.366
CAL 7		VAL 7	
N°	352	**N°**	528
m1	-15.760	**RMSE**	0.768
m0	-14.629	**BIAS_AV**	0.039
R2	0.686	**MAE**	0.418
CAL 8 50%		VAL 8 50%	
N°	440	**N°**	440
m1	-16.306	**RMSE**	0.671
m0	-15.206	**BIAS_AV**	0.049
R2	0.610	**MAE**	0.377

m0	-229.136	**BIAS_AV**	0.015
R2	0.313	**MAE**	1.214
CAL 7		VAL 7	
N°	352	**N°**	528
m1	-230.146	**RMSE**	1.466
m0	-226.262	**BIAS_AV**	0.042
R2	0.264	**MAE**	1.146
CAL 8 50%		VAL 8 50%	
N°	440	**N°**	440
m1	-242.675	**RMSE**	1.532
m0	-238.702	**BIAS_AV**	0.027
R2	0.280	**MAE**	1.188

m0	-26.742	**BIAS_AV**	-0.034
R2	0.640	**MAE**	0.387
CAL 7		VAL 7	
N°	352	**N°**	528
m1	-14.751	**RMSE**	0.740
m0	-28.196	**BIAS_AV**	0.039
R2	0.693	**MAE**	0.435
CAL 8 50%		VAL 8 50%	
N°	440	**N°**	440
m1	-15.285	**RMSE**	0.650
m0	-29.289	**BIAS_AV**	0.049
R2	0.624	**MAE**	0.396

Table 6 - Capo San Donato orthophoto results

Sentinel-2

BLUE/RED			
CAL 1		VAL 1	
N°	52	**N°**	77
m1	-3.096	**RMSE**	0.781
m0	-2.371	**BIAS_AV**	-0.250
R2	0.761	**MAE**	0.504
CAL 2		VAL 2	
N°	52	**N°**	77
m1	-4.175	**RMSE**	0.907
m0	-3.852	**BIAS_AV**	-0.201
R2	0.680	**MAE**	0.568
CAL 3		VAL 3	
N°	52	**N°**	77
m1	-5.778	**RMSE**	1.428
m0	-5.803	**BIAS_AV**	0.291
R2	0.569	**MAE**	0.928
CAL 4 50%		VAL 4 50%	
N°	65	**N°**	64
m1	-3.827	**RMSE**	0.693
m0	-3.278	**BIAS_AV**	-0.067
R2	0.625	**MAE**	0.459
CAL 5		VAL 5	
N°	52	**N°**	77
m1	-3.352	**RMSE**	0.748
m0	-2.692	**BIAS_AV**	-0.188
R2	0.724	**MAE**	0.480
CAL 6		VAL 6	
N°	52	**N°**	77
m1	-4.335	**RMSE**	0.852
m0	-3.904	**BIAS_AV**	0.089
R2	0.644	**MAE**	0.554

BLUE/GREEN			
CAL 1		VAL 1	
N°	52	**N°**	77
m1	-79.424	**RMSE**	1.255
m0	-74.854	**BIAS_AV**	-0.093
R2	0.347	**MAE**	0.924
CAL 2		VAL 2	
N°	52	**N°**	77
m1	-62.624	**RMSE**	1.111
m0	-58.512	**BIAS_AV**	0.030
R2	0.570	**MAE**	0.841
CAL 3		VAL 3	
N°	52	**N°**	77
m1	-102.061	**RMSE**	1.736
m0	-96.320	**BIAS_AV**	0.671
R2	0.173	**MAE**	1.253
CAL 4 50%		VAL 4 50%	
N°	65	**N°**	64
m1	-73.982	**RMSE**	1.137
m0	-69.543	**BIAS_AV**	-0.031
R2	0.412	**MAE**	0.828
CAL 5		VAL 5	
N°	52	**N°**	77
m1	-68.380	**RMSE**	1.075
m0	-64.082	**BIAS_AV**	0.037
R2	0.453	**MAE**	0.786
CAL 6		VAL 6	
N°	52	**N°**	77
m1	-72.226	**RMSE**	1.275
m0	-67.590	**BIAS_AV**	0.398
R2	0.528	**MAE**	0.937

BLUE/RED + BLUE/GREEN			
CAL 1		VAL 1	
N°	52	**N°**	77
m1	-2.980	**RMSE**	0.758
m0	-5.091	**BIAS_AV**	-0.244
R2	0.755	**MAE**	0.494
CAL 2		VAL 2	
N°	52	**N°**	77
m1	-3.914	**RMSE**	0.880
m0	-7.269	**BIAS_AV**	-0.187
R2	0.697	**MAE**	0.566
CAL 3		VAL 3	
N°	52	**N°**	77
m1	-5.468	**RMSE**	1.397
m0	-10.653	**BIAS_AV**	0.312
R2	0.567	**MAE**	0.914
CAL 4 50%		VAL 4 50%	
N°	65	**N°**	64
m1	-3.639	**RMSE**	0.677
m0	-6.537	**BIAS_AV**	-0.065
R2	0.634	**MAE**	0.458
CAL 5		VAL 5	
N°	52	**N°**	77
m1	-3.195	**RMSE**	0.729
m0	-5.561	**BIAS_AV**	-0.178
R2	0.729	**MAE**	0.473
CAL 6		VAL 6	
N°	52	**N°**	77
m1	-4.090	**RMSE**	0.837
m0	-7.510	**BIAS_AV**	0.106
R2	0.661	**MAE**	0.559

CAL 7		VAL 7	
N°	52	N°	77
m1	-4.943	RMSE	1.103
m0	-4.804	BIAS_AV	0.005
R2	0.557	MAE	0.697
CAL 8 50%		VAL 8 50%	
N°	65	N°	64
m1	-4.035	RMSE	0.738
m0	-3.489	BIAS_AV	0.095
R2	0.614	MAE	0.481

CAL 7		VAL 7	
N°	52	N°	77
m1	-81.465	RMSE	1.441
m0	-76.678	BIAS_AV	0.162
R2	0.344	MAE	1.078
CAL 8 50%		VAL 8 50%	
N°	65	N°	64
m1	-65.703	RMSE	0.944
m0	-61.516	BIAS_AV	-0.008
R2	0.451	MAE	0.697

CAL 7		VAL 7	
N°	52	N°	77
m1	-4.660	RMSE	1.065
m0	-8.915	BIAS_AV	0.014
R2	0.558	MAE	0.682
CAL 8 50%		VAL 8 50%	
N°	65	N°	64
m1	-3.802	RMSE	0.722
m0	-6.846	BIAS_AV	0.089
R2	0.629	MAE	0.480

Table 7 - Capo San Donato Sentinel-2 results

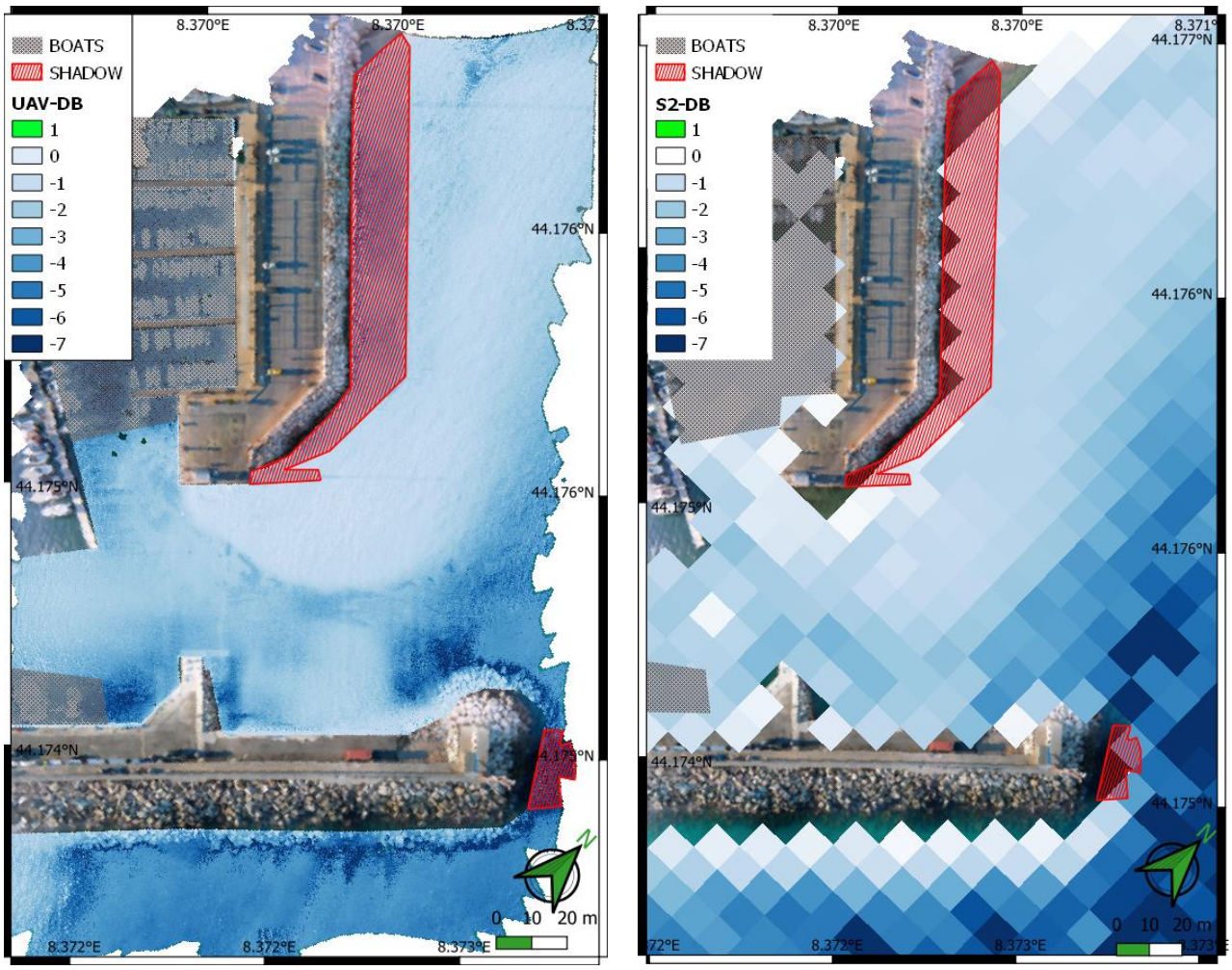

Figure 42 - Derived bathymetry for Finale Ligure using UAV orthophoto (left) and Sentinel-2 imagery (right)

Variability of statistical parameters

Concluding the results presentation, there is a last outcome to be shown. The Table 8 is related to the variability of the two main statistical parameters ($R^2$and $RMSE$). This is expressed resorting to the standard deviation of the values, computed within each iteration set of each band of each platform. Tables 9 and 10 show the average and the median of the same dataset. The median value becomes more relevant for those set of data, within which variability is higher. In fact, the satellite result is the only one to differ from its average value.

STAN.DEV.		iterations	R^2	RMSE	R^2	RMSE	R^2	RMSE
ROJA	AGEA	4	0.01	0.00	0.02	0.01	0.01	0.01
	S2	8	0.09	0.07	0.12	0.07	0.12	0.05
FINALE	UAV	8	0.03	0.05	0.03	0.06	0.02	0.04
	S2	8	0.07	0.23	0.12	0.23	0.07	0.23

Table 8 - Standard deviation of R² and RMSE for all the iterations

AVERAGE		iterations	R2	RMSE	R2	RMSE	R2	RMSE
ROJA	AGEA	4	0.80	0.30	0.70	0.39	0.78	0.31
	S2	8	0.54	0.63	0.43	0.71	0.56	0.58
FINALE	DRONE	8	0.66	0.70	0.29	1.52	0.67	0.68
	S2	8	0.65	0.91	0.41	1.25	0.65	0.88

Table 9 - Average of R² and RMSE for all the iterations

MEDIAN		iterations	R2	RMSE	R2	RMSE	R2	RMSE
ROJA	AGEA	4	0.79	0.30	0.71	0.39	0.78	0.31
	S2	8	0.51	0.62	0.43	0.68	0.52	0.58
FINALE	DRONE	8	0.67	0.71	0.29	1.52	0.68	0.69
	S2	8	0.63	0.82	0.43	1.20	0.65	0.80

Table 10 - Median of R² and RMSE for all the iterations

Results discussion

Skimming the results, we can draw our conclusions. The first thing we can underline, is that the red band seems to perform better, if compared to the green one. This depends on the considered range depth, but in our case we are dealing with small depth ranges, between 0 and 5, anyway under a limit of 10 m depth. The red spectral band is absorbed more quickly. The gradient of absorption is therefore steeper than green band's one. This determines higher efficiency in resolving the depth variations within a shallower range. As a matter of fact, the red band is the best single-band choice throughout our study, and the green one certainly is unreliable.

The double configuration, summing red ratio and green ratio, appears to be improving the results. Notwithstanding this is generally proved in the results, the sum of bands does not enhance the Roja river orthophoto result. In that case we find that the green band has satisfying values of calibration and validation. This could mean that summing the ratios is a favorable practice, when there is a larger distance between the two band ratios. This is something to be held gingerly, as we dealt with a limited depth range and, in addition, the acknowledged difference is small.

Addressing the proportion in the calibration and validation processes, we can assert that there is not a relevant difference between the 40:60 ratio and the 50:50 one. We would have expected better results when calibrating with 50% of the dataset, as the model would have been more properly fitting the circumstance. This is not to be recognized, since in some cases the calibration R^2 is even lower. The aforementioned proportion turns out to be irrelevant. Furthermore, we could observe that a good calibration is not always a proper index to infer the validation effectiveness. It can give a general idea, but the relation between calibration and validation still depends on the dataset features, like for example the outlier's relevance.

This leads us to the variability evaluation. This is a preeminent aspect of our case. The reiteration of the algorithm seems to affect the results. This is given by the different choice of dataset portions for each repetition. In our results a relevant distance between replications can be observed (Tables 5, 6, 7). This is particularly significant since we are dealing with very shallow waters. At small depths a little difference can represent a considerable problem, this is particularly true if we consider that this discrepancy is due to a simple reiteration of the initial within dataset selection. Obviously, the mentioned differences do not affect all the performed computations. Results variability is higher for satellite images, that is to say for those output, for which a lower accuracy is expected. In the case of the Roja river orthophoto analysis, no variability is to be recognized. This is evident in the Table 8 too. The standard deviation of the several reiterations shows values, that are index of potential errors, or uncertainty at least. This is true for satellite images where a 10 or 20 cm variability was computed. A change like that can be more or less significative, depending on the range of depth it is dealt with.

Exploring the numbers, which have been presented in the previous sections, we can appreciate some points. In the first place, the bias distribution diagrams (Figures 28, 32, 37). They show the subtraction of the derived value from the observed one. Generally, we can see that derived depths tend to be slightly smaller. This can be adequate, making the model more conservative. We understand that a conservative system is preferable for navigation safety, being more cautious in terms of under keel clearance. The only example where this does not happen is the Sentinel-2 dataset of Finale Ligure where, if anything, the results tend to overestimate the depth (Figure 41). The over- or underestimation is affected by the variability given by the algorithm reiterations.

There is a difference among the results, given by the properties of the used platforms. Let us overlook for an instant the sites that are interest of this study, and take into account just the used instruments. The aerial orthophotos, be they taken by a plane or a drone, served our purposes fine. The average $RMSE$ ranges from 30 cm to 70 cm for the best-performing band (Table 9). On the other hand, a lower accuracy is produced by satellite imagery

processing, for whom the $RMSE$ ranges from 60 cm to 90 cm. These would be an outstanding outcome if they were relative to a wider range of depth, commonly 0 to 20 m. In our case it is a regular result providing a fair remote measurement. In addition, the satellite derived $RMSE$ is subject to a higher variability due to the algorithm reiterations: from a cycle to another the final bathymetry for Finale Ligure can differ of more than 20 cm. From the graphical point of view, the satellite output tends to smooth the bathymetry because of its spatial resolution, that does not allow to gather abrupt variations.

Concerning the discrepancies between the river mouth environment and the coastal one, the Roja river gets better results. The numbers are more accurate and precision is higher, as variability is lower. The aerial orthophoto of the Roja river shows the best result. The accuracy is high, and the output can be used reliably. Even green band can be helpful, as the sum of bands does not increase the closeness to real data. The satellite data for the Roja river are represented at their best by the sum of ratios. This produced a quite good accuracy, under 50 cm of $RMSE$. Moving to the coastal zone of the marina in Finale Ligure, at Capo San Donato, we get worse results than before. In the case of the UAV orthophoto this could be ascribed to the water clearness, allowing the bottom structures, like ripple marks, to be half-seen. This could have produced an interference effect. Another fact, perhaps having larger influence, is the involved number of points. If in the Roja river orthophoto we can rely on more than 3000 points, here we have 880 ones. The area dimensions are obviously different but, in a considering proportions computation, the dissimilitude in the points number could have played a major role. Looking at the Sentinel-2 data for Finale Ligure we see that they get worse at first sight. However, those numbers are consistent with those from the river. The difference with their aerial counterpart, the orthophotos, is constant at approximately 20 cm $RMSE$. Summing up, the Roja river gives better results than the coastal marina in Finale Ligure, but the usage of satellite seems to equally indulge the unlike properties of the studied sites.

We explored results and outcomes. We get that the central idea is that the choice of the starting image is crucial. We have seen how important the structure of extracted data can

be, to obtain an accurate final development. Surely the conditions of the site of interest are important, but the snapshots we get of it, can really make the difference between a decent job and a very good one. Lights, shades, reflections, turbidity, resolution are all aspects to be considered when taking or downloading the to be processed imagery.

What could be enhanced, if repeating this work? The involved sites were not conceived as parts of the same comparative project and this could have affected the result. If the work should be started over again, a better preliminary planning phase would improve its effectiveness. The contemporaneity of the several surveys (SBES, UAV, satellite passages) is a difficult but substantial point in any field research activity. A simultaneous acquisition of data would make the dataset more robust, so the result.

Conclusions

The present study focuses on the calculation of coastal and river bathymetry models from in situ measurements needed to calibrate an empirical algorithm, using aerial orthophotos and satellite images.. The results demonstrate the used instruments can provide a variable accuracy degree. This is said for the conditions to be faced as for each instrument itself. The specs of each tool make it suitable for some particular utilizations. The UAV can improve resolution, the satellite can increase synoptic view, and the SBES/MBES provides accuracy. The state of the art of satellites and UAVs was addressed, defining a place for these technologies in future research activities. However, the direct measurement, in a representative area, is essential when using an empirical algorithm.

This study has loaded new questions along the way. For instance, about the algorithm to be used, as some machine learning one seems to perform better for SDB (Wei et al., 2021). Or about the automation of the process that could be completely realized in python, taking advantage of the libraries referred to SNAP-ESA (snappy - ESA) and the QGIS API (QGIS Development Team, n.d.-a), and resorting to in-built ones like Pandas (McKinney, 2011)

and NumPy (Harris et al., 2020) to manage the computation of the final outputs. The introduction of recursion into the chosen algorithm could lead to a progressive refinement of the result.

Bearing in mind what has been said up to now, it is now time for us to answer our original question. The satellite and the remote sensing in general cannot be considered as reliable as a traditional method, namely a direct hydrographic survey. This said, it can be successfully used to produce integration data, or stand-alone results when not extreme accuracy is required. This is particularly true when attention is given to a variety of factors, such as resolution, weather conditions, quality of the taken picture, number of points etc. The integration is always needed when the survey includes not navigable areas, maybe due to shallow waters or rocky coasts, or to seamounts if operations are carried out offshore. The remote sensing is useful to measure the 0 m depth zones too. Remote sensing is a relevant ally in the pursuit of the accuracy and completeness of any survey. Nevertheless, we have seen that this branch is not uniform. Aerial orthophotos can provide us with outstanding resolutions, while satellites can cover distant area providing its peculiar synoptic perspective. Their usage is to be decided in accordance with the prerequisites of the survey. The future holds enhancements undoubtedly. In the coming years remote sensing, in all its declination, is intended to grow and expand its application fields. Satellites are going to play a major role in each one of them. The whole world can rely on these orbiting instruments that, for the mentioned purposes, are available for everybody, significantly for those country needing to fill up the technological and cartographical gap but hampered by shortage of funds.

Bibliography

Bibuli, M., Ferretti, R., Odetti, A., & Cosso, T. (2021). River Survey Evolution by means of Autonomous Surface Vehicles. *2021 International Workshop on Metrology for the Sea; Learning to Measure Sea Health Parameters (MetroSea)*, 412–417. https://doi.org/10.1109/MetroSea52177.2021.9611629

Borra, S., Thanki, R., & Dey, N. (2019). *SPRINGER BRIEFS IN APPLIED SCIENCES AND TECHNOLOGY - COMPUTATIONAL INTELLIGENCE Satellite Image Analysis: Clustering and Classification*. Springer. http://www.springer.com/series/10618

Brockmann Consult. (n.d.). *snappy SNAP-Python module of ESA's Sentinel Applcation Platform (SNAP)*.

Casal, G., Monteys, X., Hedley, J., Harris, P., Cahalane, C., & McCarthy, T. (2019). Assessment of empirical algorithms for bathymetry extraction using Sentinel-2 data. *International Journal of Remote Sensing*, *40*(8), 2855–2879. https://doi.org/10.1080/01431161.2018.1533660

Coveney, S., & Monteys, X. (2011). Integration potential of INFOMAR airborne LIDAR bathymetry with external onshore LIDAR data sets. *Journal of Coastal Research*, *62*, 19–29.

Dayem, A., & Akter, A. (2020, August 27). Mapping river bathymetry using Stumpf model. *IABSE-JSCE Joint Conference on Advances in Bridge Engineering-IV. Definitive Outcomes for the People*.

ESA. (n.d.-a). *SNAP - ESA Sentinel Application Platform v2.0.2*. Retrieved March 1, 2023, from http://step.esa.int

ESA. (n.d.-b). *User guides - Sentinel Online*. Retrieved March 6, 2023, from https://sentinels.copernicus.eu/web/sentinel/user-guides/sentinel-2-msi/resolutions/spatial

European Space Agency Site. (2022). *ESA - https://www.esa.int, visited 1st February 2022*.

Gao, J. (2009). Bathymetric mapping by means of remote sensing: methods, accuracy and limitations. *Progress in Physical Geography*, *33*(1), 103–116.

Harris, C. R., Millman, K. J., van der Walt, S. J., Gommers, R., Virtanen, P., Cournapeau, D., Wieser, E., Taylor, J., Berg, S., & Smith, N. J. (2020). Array programming with NumPy. *Nature*, *585*(7825), 357–362.

International Hydrographic Organization. (2020). *S-44, Standards for Hydrographic Surveys Ed.6* (6.0.0). https://iho.int/uploads/user/pubs/standards/s-44/S-44_Edition_6.0.0_EN.pdf

Kara, A. B., Wallcraft, A. J., & Hurlburt, H. E. (2005). A new solar radiation penetration scheme for use in ocean mixed layer studies: An application to the Black Sea using a fine-resolution hybrid coordinate ocean model (HYCOM). *Journal of Physical Oceanography*, *35*(1), 13–32.

Legleiter, C. J., Roberts, D. A., & Lawrence, R. L. (2009). Spectrally based remote sensing of river bathymetry. *Earth Surface Processes and Landforms*, *34*(8), 1039–1059. https://doi.org/10.1002/esp.1787

Lyzenga, D. R. (1978). Passive remote sensing techniques for mapping water depth and bottom features. *Applied Optics*, *17*(3), 379. https://doi.org/10.1364/ao.17.000379

Lyzenga, D. R., Malinas, N. P., & Tanis, F. J. (2006). Multispectral bathymetry using a simple physically based algorithm. *IEEE Transactions on Geoscience and Remote Sensing*, *44*(8), 2251–2259. https://doi.org/10.1109/TGRS.2006.872909

McKinney, W. (2011). pandas: a foundational Python library for data analysis and statistics. *Python for High Performance and Scientific Computing*, *14*(9), 1–9.

Monteys, X., Harris, P., Caloca, S., & Cahalane, C. (2015). Spatial prediction of coastal bathymetry based on multispectral satellite imagery and multibeam data. *Remote Sensing*, *7*(10), 13782–13806. https://doi.org/10.3390/rs71013782

Mumby, P. J., Clark, C. D., Green, E. P., & Edwards, A. J. (1998). Benefits of water column correction and contextual editing for mapping coral reefs. *International Journal of Remote Sensing*, *19*(1), 203–210.

Niroumand-Jadidi, M., Bovolo, F., & Bruzzone, L. (2020). SMART-SDB: Sample-specific multiple band ratio technique for satellite-derived bathymetry. *Remote Sensing of Environment*, *251*. https://doi.org/10.1016/j.rse.2020.112091

Pe'eri, S., Parrish, C., Azuike, C., Alexander, L., & Armstrong, A. (2014). Satellite remote sensing as a reconnaissance tool for assessing nautical chart adequacy and completeness. *Marine Geodesy*, *37*(3), 293–314.

Pizzeghello, N. M., & Sinapi, L. (2022). Hydrography: From Marine Data to Information. In *Measurement for the Sea: Supporting the Marine Environment and the Blue Economy* (pp. 1–25). Springer.

Polcyn, F. C., Brown, W. L., & Sattinger, I. J. (1970). *The measurement of water depth by remote sensing techniques*. Michigan Univ Ann Arbor Inst of Science and Technology.

QGIS Development Team. (n.d.-a). Geographic Information System API Documentation. In *QGIS Association*. Retrieved March 1, 2023, from https://qgis.org/pyqgis/3.22/index.html

QGIS Development Team. (n.d.-b). *QGIS Geographic Information System*. QGIS Association. Retrieved March 1, 2023, from https://www.qgis.org

Regione Liguria. (2005). *Sistema informativo regionale ambientale della Liguria - SIRAL*. https://ambientepub.regione.liguria.it/SiraQualMeteo/script/PubAccessoDatiMeteo.asp

Regione Liguria. (2020). *Aggiornamento del sistema di allertamento e linee guida per la pianificazione del livello comunale e provinciale di Protezione Civile - "Libro Blu" - aggiornamento 2020*. https://www.regione.liguria.it/components/com_publiccompetitions/includes/download.php?id=45574:libro-blu-2020.pdf

Robinson, I. S. (1983). Satellite observations of ocean colour. *Philosophical Transactions of the Royal Society of London. Series A, Mathematical and Physical Sciences*, *309*(1508), 415–432.

Salavitabar, S., Li, S. S., & Lak, B. (2022). Mapping Underwater Bathymetry of a Shallow River from Satellite Multispectral Imagery. *Geosciences (Switzerland)*, *12*(4). https://doi.org/10.3390/geosciences12040142

Serco Italia SPA. (2021). *Nearshore Bathymetry Derivation with Sentinel-2. (version 1.1). Retrieved from RUS Lectures*. https://rus-copernicus.eu/portal/wp-content/uploads/library/education/training/COAS01_BathymetryDerivation_Greece.pdf

Stumpf, R. P., Holderied, K., & Sinclair, M. (2003). Determination of water depth with high-resolution satellite imagery over variable bottom types. *Limnology and Oceanography*, *48*(1 II), 547–556. https://doi.org/10.4319/lo.2003.48.1_part_2.0547

The Mathworks Inc. (2022, October 26). *MATLAB version 9.13.0.2105380 (R2022b)*. Natick, Massachusetts. https://it.mathworks.com/

Wei, C., Zhao, Q., Lu, Y., & Fu, D. (2021). Assessment of empirical algorithms for shallow water bathymetry using multi-spectral imagery of pearl river delta coast, China. *Remote Sensing*, *13*(16). https://doi.org/10.3390/rs13163123

Wezernak, C. T., & Lyzenga, D. R. (1975). Analysis ofCladophora distribution in Lake Ontario using remote sensing. *Remote Sensing of Environment*, *4*, 37–48.

Winterbottom, S. J., & Gilvear, D. J. (1997). Quantification of channel bed morphology in gravel-bed rivers using airborne multispectral imagery and aerial photography.

Regulated Rivers: Research and Management, *13*(6), 489–499. https://doi.org/10.1002/(SICI)1099-1646(199711/12)13:6<489::AID-RRR471>3.0.CO;2-X

Yang, H., Kong, J., Hu, H., Du, Y., Gao, M., & Chen, F. (2022). A review of remote sensing for Water Quality Retrieval: Progress and challenges. *Remote Sensing*, *14*(8), 1770.

List of Figures

List of Tables